1. BASIC INFORMATION

Title : Novel Nanophosphors for High Efficiency Fluorescent Lamps

Type of report: Final Report

Reporting Period Start Date: 10/1/2003

Reporting Period End data: 6/30/2007

Principle Author: Alok M. Srivastava

Date Report was issued: June 28, 2007

DOE Award number: DE-FC26-03NT41945

Name and Address of Submitting Organization:

GE Global Research, One Research Circle, Niskayuna, NY 12309

2. DISCLAMER

3. ABSTRACT

This is the Final Report of the Novel Nanophosphors for High Efficiency Fluorescent Lamps, Department of Energy (DOE). The overall goal of this three-year program is to develop novel hybrid phosphors by coating commercially available lamp phosphors with highly stable wide band-gap nanocrystalline phosphors (NCP). The prime technical approach is the development of NCP quantum-splitting phosphor (QSP) and ultra-violet (UV) emitting phosphors with quantum efficiencies exceeding that of the conventional phosphors at 185 nm. The novel hybrid phosphors will increase the efficiency of the fluorescent lamps by up to 32%, enabling total energy savings of 0.26 quads, the reduction in the U.S. energy bill by $6.5 billion and the reduction of the annual carbon emission by 4.1 billion kilogram.

Our work started by investigating through modeling calculations the requirement for the particle size of the NCP. Our work to develop suitable nanocrystalline phosphors started with the known oxide quantum splitting and UV emitting phosphors. We demonstrated several synthesis techniques for the production of high quality nanocrystalline materials that crystallizes in the desired phase and with the desired particle size. In collaboration with our subcontractor we demonstrated the feasibility for the manufacture of NC phosphors. We also demonstrated novel techniques of coating the NCP on the surface of micron sized phosphors.

Our chief achievement pertains to the successful testing of the coated hybrid phosphor systems in linear fluorescent lamps. In linear fluorescent lamp tests, we have demonstrated up to 7% increase in the efficacy of hybrid phosphors over the conventional (uncoated) phosphors. We have also demonstrated the improvement in the lumen maintenance of the coated phosphors. A hybrid phosphor system based on the commercial red emitting phosphor, $Y_2O_3:Eu^{3+}$ did not show the anticipated improvement in lamp efficacy. We explored the reasons for this observation, which are detailed in this report.

Within the program we have carried out fundamental investigations into the physical processes that determine the quantum splitting behavior of the Pr^{3+} ion in solids. Specifically, we have investigated the quantum splitting luminescence of this ion in the $LaPO_4$, $SrAl_{12}O_{19}$ and $LiLaP_4O_{12}$ host lattices.

In this final report we summarize the technical work completed under the Program, summarize our findings about the performance limits of the various technologies we investigated, and outline promising paths for future work.

TABLE OF CONTENT

4. LIST OF GRAPHICAL MATERIALS

Figure 13: The normalized and corrected luminescence spectra of the nanocrystalline and microcrystalline (insert) $SrAl_{12}O_{19}$:1% Pr, Mg samples at 10 (bottom) and 290 K (top).

Figure 14: Typical relaxation curve of the $^1S_0$ to $^1I_6$ transition of nanocrystalline sample recorded at 10 K (the detection wavelength is 405 nm).

Figure 15: the $^1S_0$ relaxation time as a function of temperature for nano and micron sized $SrAl_{12}O_{19}$:1% Pr, Mg sample.

Figure 16: The excitation spectra of the nano- and microcrystalline $SrAl_{12}O_{19}$:1% Pr, Mg at room-temperature normalized to the signal maxima.

Figure 17: the XRD of LAP samples synthesized by using various surfactant.

Figure 18: The TEM of the ultraviolet emitting LAP ($LaPO_4:Pr^{3+}$) phosphor produced by two different surfactant.

Figure 19 : Synthesis route, XRD and TEM of the 10 nm $LaPO_4$ phosphor particles

Figure 20: X-ray diffraction patterns of the quantum splitting $LaB_3O_6:Pr^{3+}$ phosphor. The particle size is indicated in the Figure.

Figure 21: The TEM of the quantum splitting $LaB_3O_6:Pr^{3+}$ phosphor.

Figure 22: The XRD of LaB_3O_6 samples synthesized by using various surfactant. The particle sizes are indicated in the figure.

Figure 23: The room temperature emission spectrum of the nanocrystalline Quantum splitting phosphor $LaB_3O_6:Pr^{3+}$

Figure 24: SEM of nano particles synthesized under two different conditions. The particles on the left are highly aggregated and particles on the right are well dispersed. Note the needle like morphology of the particles.

Figure 25: Zeta potential values over a range of pH for the core particle and the nano phosphor particles.

Figure 26: Transmission electron micrograph of coated particles (a) well-dispersed precursor and (b) aggregated precursor.

Figure 27: Transmission electron micrograph of coated particles using well-dispersed precursor.

Figure 28: Transmission electron micrograph of double coated particles using well-dispersed precursor.

Figure 29: Transmission electron micrograph of precursor particles synthesized by a propriety technique.

Figure 30: The X-ray diffraction pattern of the precursor material showing the attainment of particles with 31 nm particle size.

Figure 31: Transmission electron micrograph of coated core particles

Figure 32: Schematic experimental procedure for in-situ coating technical approach (Top), and ex-situ coating technical approach (Bottom)

Figure 33: X-ray diffraction, transmission electron microscopy, and energy dispersive spectroscopy analysis for samples of $LaPO_4$:Pr coated onto Y_2O_3:Eu micron size particles using an ex-situ coating technical approach.

Figure 34. Schematic drawing of the small, pilot-plant scale, production line of fine ceramic powderd. (Green arrows indicate the flow of powders in the production line).

Figure 35 : SEM pictures of as-received YEO particles (commercial phosphor)

Fig. 36 XRD profile of YEO powders coated with $La_{0.99}Pr_{0.01}PO_4$ particles fabricated by flame processing based on the PVA method.

Fig. 37. SEM micrographs of YEO powders coated with $La_{0.99}Pr_{0.01}PO_4$ particles fabricated by flame processing based on the PVA method.

Figure 38. SEM micrographs of YEO powders coated with half amounts of $La_{.99}Pr_{0.01}PO_4$ particles compared to those shown in Fig. 37.

Figure 39: The plasma torch assembly

Figure 40: Experimental condition for the synthesis of SAP samples

Figure 41: Experimental condition for the synthesis of LAMB samples

Figure 42: Schematic of the reaction assembly to produce nano particles

Figure 43: The room temperature emission spectrum of the Quantum splitting phosphor $SrAl_{12}O_{19}:Pr^{3+}$ phosphor from precursors obtained from TAL Materials, Inc. (green: as-obtained material; blue: fired at 1000C for five hours; red: fired at 1000 C for 120 hours).

Figure 44: X-ray diffraction patterns of the quantum splitting $SrAl_{12}O_{19}:Pr^{3+}$ phosphor from precursors obtained from TAL Materials, Inc. The precursors were heated to various temperatures/time. The particle size is indicated in the Figure.

Figure 45: Room temperature emission spectrum of $La_{0.999}Pr_{0.001}PO_4$ at T= 300 K (λ_{ex}= 193 nm).

Figure 46: Emission spectrum of $La_{0.999}Pr_{0.001}PO_4$ at T= 1.6 K (λ_{ex}= 193 nm).

Figure 47: High-resolution emission spectrum of $La_{0.999}Pr_{0.001}PO_4$ at T= 1.6 K (λ_{ex}= 193 nm).

Figure 48: The excitation spectrum of $La_{0.999}Pr_{0.001}PO_4$ at T= 10 K for $4f^15d^1$ and ^1S_o emission

Figure 49: The $^1S_0$ decay curves in $La_{0.999}Pr_{0.001}PO_4$ at T= 10 K and T= 1.7 K

Figure 50: The temperature dependence of the $^1S_0$ relaxation time in $La_{0.999}Pr_{0.001}PO_4$ (see text for the model)

Figure 51: A schematic configuration coordinate model for the luminescence of Pr^{3+} in $LaPO_4$

Figure 52: The excitation spectrum of $LiLa_{0.999}Pr_{0.001}P_4O_{12}$ at T= 10 K (λ_{em}= 406 nm)

Figure 53: The emission spectra of $LiLa_{0.999}Pr_{0.001}P_4O_{12}$ at various temperatures (λ_{ex}= 210 nm)

Figure 54: The temperature dependence of the Pr^{3+} $^1S_0 \rightarrow {}^1I_6$ (λ_{em} = 405 nm) lifetime in $LiLaP_4O_{12}$. The excitation wavelength was 193 nm. The full circles are the experimental points and the solid curve is the theoretical fit (see text).

Figure 55: TEM of $YVO_4:Eu^{3+}$ commercial phosphor coated with nanophosphor $LaPO_4:Pr^{3+}$. A very uniform coating of the nanophosphor is evident from the TEM image.

Figure 56: TEM of $YVO_4:Eu^{3+}$ commercial phosphor coated with nanophosphor $LaPO_4:Pr^{3+}$. The coating of the nanophosphor is not uniform.

Figure 57: TEM of $YVO_4:Eu^{3+}$ commercial phosphor coated with nanophosphor $LaPO_4:Pr^{3+}$. The coating of the nanophosphor is very poor.

Figure 58: The lamp performance of NN 0815 sample (0-100h.). Note the improved zero and 100 h. performance of the hybrid phosphor and the improved lumen maintenance.

Figure 59: The lamp performance of NN 1221 sample (0-1000h.). Note that at 100 h. the efficacy of the hybrid and the commercial phosphors are the same. However, the hybrid phosphor exhibits much improved lumen maintenance in the 100 h- 1000 h time range.

Figure 60: The lamp performance of NN 0112 sample (0-1000h.). The poor lamp performance of this hybrid phosphor can be related to the very poor outer coating of the nanophosphor.

Figure 61: TEM of Y_2O_3:Eu^{3+} commercial phosphor coated with nanophosphor $LaPO_4$: Pr^{3+}. The coating of the nanophosphor is uniform. Despite the uniform coating, the absorption of the phosphor for 254 nm radiation is only 46%. The absorption of the core Y_2O_3:Eu^{3+} phosphor is 64% (see text).

Figure 62: TEM of Y_2O_3:Eu^{3+} commercial phosphor coated with nanophosphor $LaPO_4$: Pr^{3+}. The coating of the nanophosphor is uniform. Despite the uniform coating, the absorption of the phosphor for 254 nm radiation is only 41%. The absorption of the core Y_2O_3:Eu^{3+} phosphor is 64% (see text).

Figure 63: The lamp performance of NN 203 And NN 216 samples (0-1000h.). The poor lamp performance of this hybrid phosphor can be related to the high reflectivity (254 nm) of the outer coating of the nanophosphor.

Figure 64: TEM of Y_2O_3:Eu^{3+} commercial phosphor coated with a single coat of the nanophosphor $LaPO_4$: Pr^{3+}. The coating of the nanophosphor is thin and uniform. The absorption of the phosphor for 254 nm radiation is improved to 59%.

Figure 65: TEM of Y_2O_3:Eu^{3+} commercial phosphor coated with a double coat of the nanophosphor $LaPO_4$: Pr^{3+}. The coating of the nanophosphor is uniform. The absorption of the phosphor for 254 nm radiation has dropped to 49%.

5. INTRODUCTION

The overall goal of this program is to reduce energy consumption and concurrently reduce pollution by developing novel hybrid phosphor system based on nanocrystalline quantum splitting and ultraviolet emitting phosphors with quantum efficiencies exceeding that of the conventional phosphors at 185 nm. By combining advanced phosphors and innovating system modeling for full optimization, we believe we can further increase the efficiency of fluorescent lamps with the use of quantum-splitting phosphors which, on average, produce more than one visible photon for each incident ultraviolet photon.

Our project goals and the technical paths we have pursued are driven by our desire to closely approximate conventional fluorescent lamps in form, cost and manufacturing process. A 40 W fluorescent lamp has intrinsic losses in the conversion from electrical power to Hg plasma radiation of ~15 W, producing 7 W and 17 W of 185 nm and 254 nm radiation, respectively. GE 's optimized micron-sized triphosphor blend converts this 254 nm radiation into 8 W of visible light. The majority of the energy loss comes from the large Stokes shift from converting 254 nm radiation into visible light; since quantum efficiencies (QEs) for high efficiency phosphors are greater than 90% at 254 nm, further increases in this efficiency are unlikely. However, the 185 nm radiation is converted into only 1 W of visible light. This is partially due to the larger Stokes shift, but also results from the lower QE excitation (about 70% for the white light emitting triphosphor blend). Consequently, if there is any hope of significantly increasing the efficacy of linear fluorescent lamps we have to focus our attention to the more efficient conversion of the 185 nm radiation of the mercury discharge. To improve the conversion efficiency of the 185 nm radiation, we took into consideration the development of quantum splitting phosphors, which, on average, produce more than one visible photon for each incident ultraviolet photon.

GE has led in the discovery and understanding of these materials through their previous DOE contract for Next- Generation High Efficiency Lighting products (Contract No. #DE-FC26-99FT40632). However, even though QSPs can have QEs greater than unity, adding them as micron-sized powders to fluorescent lamp coatings leads to significant scattering of the 254nm radiation back into a weakly absorbing Hg-plasma. In addition, current QSPs, emit in the UV and deep blue spectral region, where the lumen equivalent is very low. To realize the full benefits of QSPs in current Hg-based fluorescent lamps, a novel hybrid phosphor system composed of nanosized QSPs coating highly efficient micronsized conventional triphosphor particles must be realized by:

• Development of nanocrystalline phosphors(NCPs) with high QE under 185 nm radiation and size distribution (5-50 nm) that minimizes scattering of 254 nm radiation.

• Integration of these phosphors into a hybrid phosphor system where the NCP is coating the conventional, micron-size lighting phosphors (Figure 4) to convert all NCP emissions into useful visible light.

In the hybrid phosphor system, the 185 nm photons from the Hg discharge are absorbed and efficiently converted into visible and UV light by the NCP coating layer (Figure 1). The 254 nm photons from the Hg discharge and the UV QSP emission will pass through the NCP layer and excite the underlying conventional phosphorparticle. These novel hybrid phosphor systems can simultaneously optimize the conversion efficiency of 185 nm and 254 nm radiation from the Hg discharge into useful visible light, and meet the stringent requirements for high quality lighting sources.

We also considered the development of efficient ultraviolet emitting phosphors, which exhibit higher quantum efficiency under 185 nm radiation than the current triphosphor blend of the conventional fluorescent lamp. However, even though the quantum efficiency of the proposed quantum-splitting and the ultraviolet emitting phosphors is higher, the simple addition of these phosphors with particle size in the micrometer range to the conventional phosphor blend results in the strong scattering of the 254 nm radiation. This scattering event is detrimental to the overall lamp performance (lumen output). Consequently, the goal of the program is unattainable with large particle size of the new phosphors. To realize the full benefit of the quantum splitting and ultraviolet emitting phosphors, a novel hybrid phosphor system composed of nanocrystalline quantum-splitting/ultraviolet emitting phosphors coating the highly efficient triphosphor particles must be realized (see Figure 1). Thus, our main effort pertains to the development of nanocrystalline phosphors with high quantum efficiency at 185 nm excitation and with size distribution that minimizes the scattering of the 254 nm radiation.

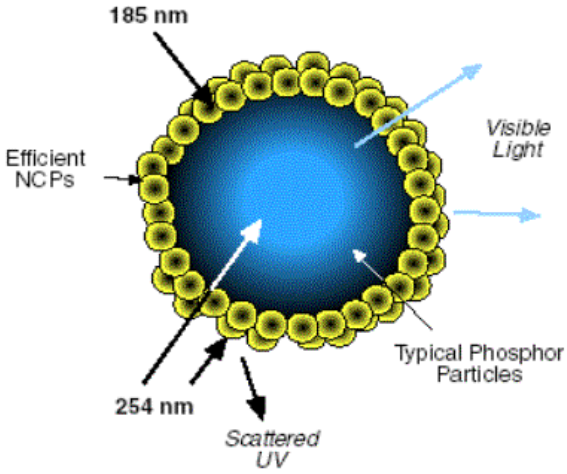

Figure 1: Schematic of the hybrid phosphor system. The NCP will efficiently convert the 185 nm Hg radiation into visible radiation while minimally scattering the 254 nm and the visible radiation generated by the micron sized phosphor.

This Program will provide benefit to the entire lighting industry and beyond. Achievement of the project goals will save money for US end-users, while the whole country will benefit from reduced energy consumption and pollution from fossil fuel

power plants. The estimated reduction in national energy consumption through use hybrid phosphor system based on quantum-splitting phosphors is 0.26 quads. The novel hybrid phosphors will increase the efficiency of the fluorescent lamps by up to 32%, enabling total energy savings of 0.26 quads, while the estimated reduction of the annual carbon emission by 4.1 billion kilogram.

Several major work of this program are formally subcontracted outside GE. Figure 2 exhibits the summary of DOE nanophosphor program including the major players. The summary of the tasks undertaken within the DOE program is shown in Figure 3. The optical characterization of quantum-splitting phosphors which included the measurement of excitation and emission spectrum under vacuum ultraviolet radiation and the determination of radiative and nonradaitive transitions was subcontracted to Prof. U. Happek at the University of Georgia. TAL MATERIALS, INC., which is a recognized leader in the development of oxide nanoparticles, is subcontracted for the manufacturing of the identified nanocrystalline phosphors. Clarkson University, which is recognized leader in the handling and coating of nanocrystalline phosphors is subcontracted for the development of coatings of the nanocrystalline phosphors on the micron sized conventional phosphors.

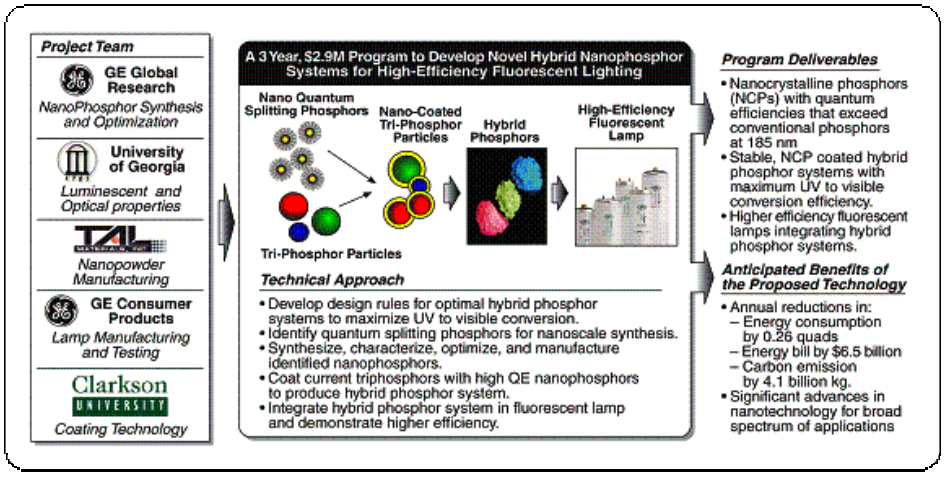

Figure 2: A summary of the DOE funded nanophosphor program

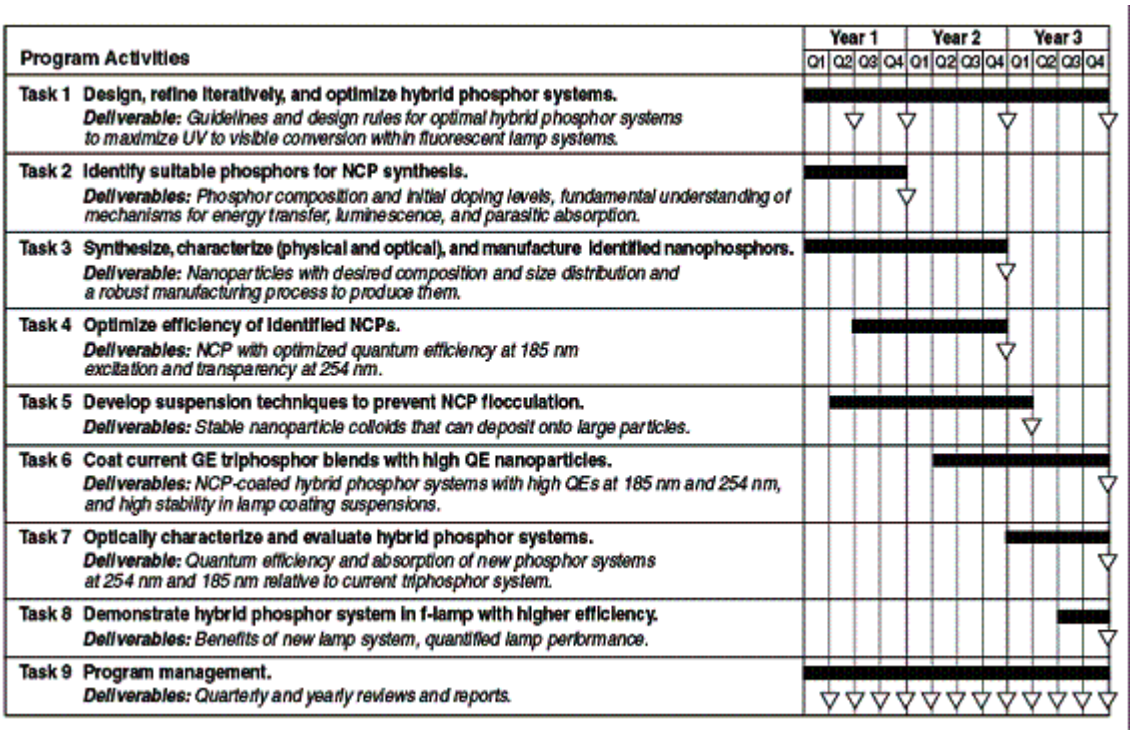

Figure 3: Summary of the tasks undertaken within the DOE program

6. ENERGY SAVINGS AND CARBON EMISISON REDUCTION

Taking into account the efficiency of different lamp types, the novel hybrid phosphor system will have 32% higher efficiency when compared to lamps with halophosphate phosphor (70 lm/W) and 10% higher efficiency when compared to lamps using rare earth based phosphors (85-100 lm/W). As shown in Figure 4, this technology enables a total national energy savings of 0.26 quads and energy bill reduction of $6.5 billion annually. With an estimated total energy savings of 0.26 quads, the corresponding annual reduction in power plant carbon emission is 4.1 billion kilograms (Figure 5).

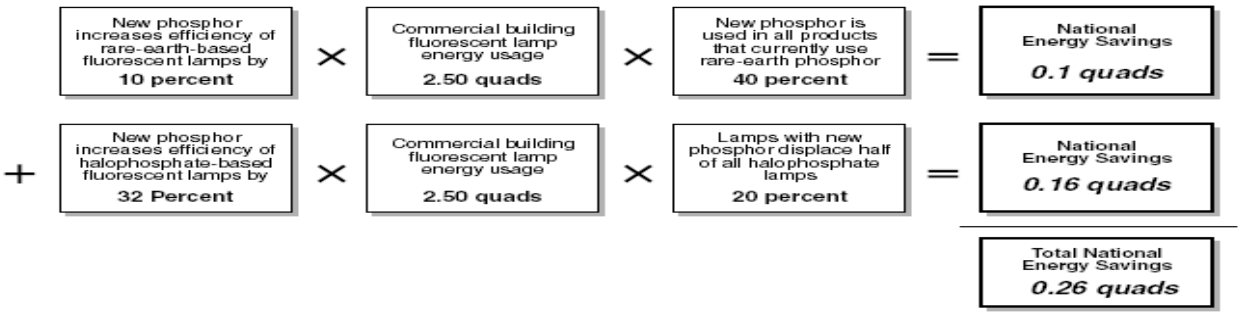

Figure 4: Energy savings from the proposed hybrid phosphor system. Anticipated market penetration would lead to an energy savings as high as 0.26 quads and energy bill reduction of $6.6 billion annually.

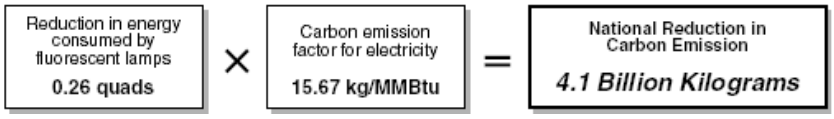

Figure 5: Carbon emission reduction. With an estimated total energy savings of 0.26 quads, the corresponding annual reduction in power plant carbon emission is 4.1 billion kilograms

7.0 Detailed description of work performed on each task

7.1 Design, refine iteratively, and optimize hybrid phosphor systems

Modeling calculations for the required particle size

We describe the modeling calculations that were performed for determining the requirement of the particle size. Our calculations are based upon a geometry where 185/254 nm radiation first interacts with a nanoparticle layer before the micron sized phosphor particles. In this calculation, the nanoparticle layer absorbs at least 75% of the 185 nm light incident on the hybrid phosphor system. Using these assumptions, Mie scattering based code was then used to determine the absorption and scattering coefficients for individual nanophosphor particles (www.omlc.org). These values were then used to calculate the required thickness of the nanophosphor layer and the reflection and transmission of the 254 nm radiation through the nanophosphor layer was calculated. Both of these calculations used on-line code for van de Hulst's adding-doubling algorithm (www.omlc.org). We then estimated the lamp performance data from GE Lighting data for the scattering losses and the results of our modeling calculations is shown in Figure 6. It is clear that for a quantum efficiency of 120 percent, the mean diameter of the nano phosphor must be less than about 100 nm.

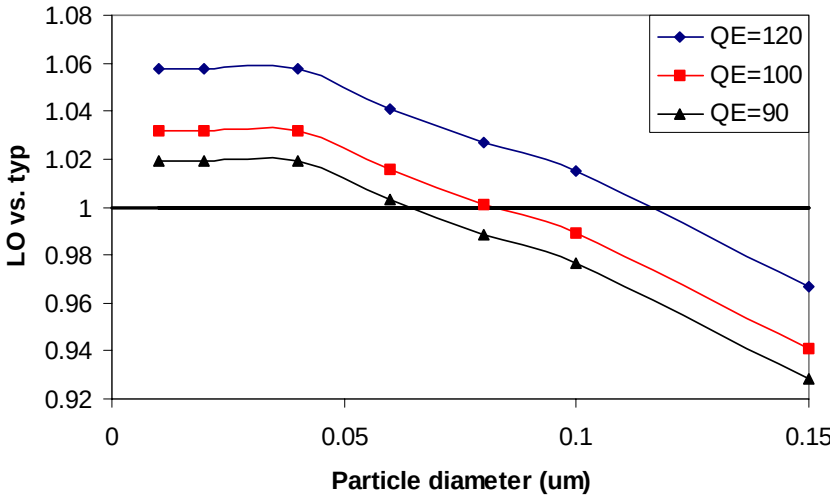

Figure 6: The dependence of the light output (against standard) on the particle size for 185 nm excitation of phosphors with quantum efficiencies of 120%, 100% and 90%, respectively.

7.2 Identify suitable phosphors for NCP synthesis

This section will be devoted to a summary of the work performed as a part of the project on identification, synthesis and testing of various nanocrystalline phosphor materials. Our materials are based on the UV or the quantum splitting emission on the Pr^{3+} ion, the energy structure of which is shown in Figure 7.

A number of quantum-splitting and UV emitting phosphors were identified for synthesis and compositional optimization work: $SrAl_{12}O_{19}:Pr^{3+}$, $LaB_3O_6:Pr^{3+}$, $LaMgB_5O_{10}:Pr^{3+}$, $LaPO_4:Pr^{3+}$, $CaAl_4O_7:Pr^{3+}$, $SrB_4O_7:Pr^{3+}$. Apart from the previously identified compositions, we have also discovered several new Pr^{3+} compositions that can be used as UV-emitting nanophosphors within our hybrid phosphor concept. Examples of such materials include $LaBO_3:Pr^{3+}$, $CaBPO_5:Pr^{3+}$, and $YBO_3:Pr^{3+}$ (Figure 8). The crystal chemistry parameters for these materials (i.e. bond length, coordination number, coordination polyhedra) will be used to develop rules for efficient Pr^{3+} UV emission in oxide hosts, similar to previous rules for quantum splitting phosphors. Further work is necessary to evaluate the quantum efficiency of these materials. In addition, we have also discovered another new oxide based quantum-splitting phosphor, $NaLa(SO_4)_2:Pr^{3+}$ (Figure 8). This material cannot be used in conventional Hg fluorescent lamps due to the presence of Na^+ and S^{6+}, both of which will readily react with Hg. However, it provides the ability to further refine our crystal chemistry rules for efficient quantum splitting phosphors in oxide hosts.

From our phosphor identification work, we down selected two materials for the coating experiments. The first material, $LaPO_4:Pr^{3+}$ emits broad band UV emission with a quantum efficiency approaching unity when excited by 185 nm (Figure 9). The second material, $SrAl_{12}O_{19}:Pr^{3+}$ is the well known quantum splitting phosphor. In the following we will describe the attainment of high quality nano particles of these materials as well as result obtained on producing the hybrid phosphor.

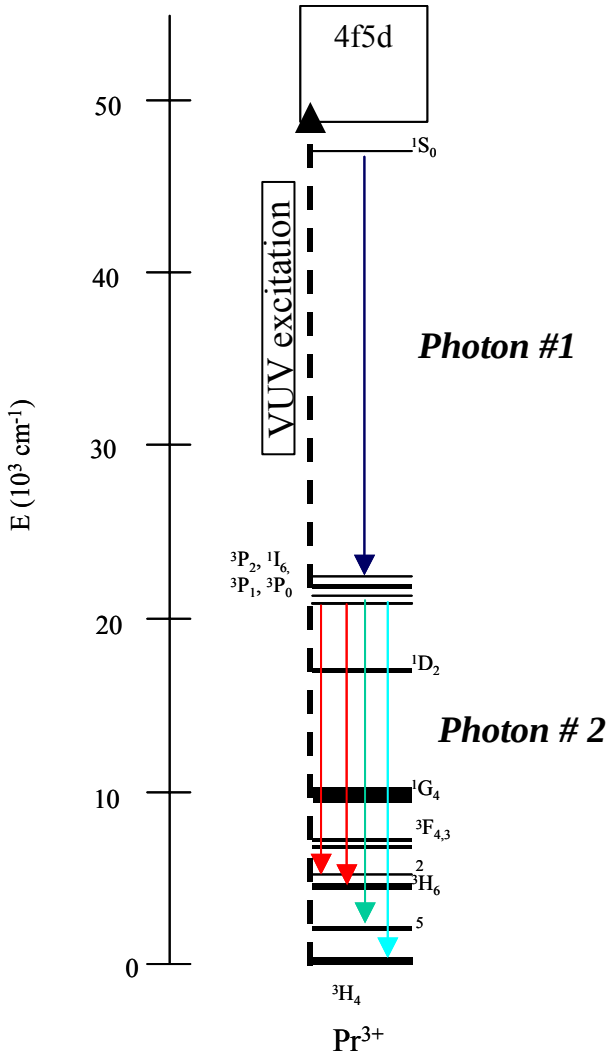

Figure 7: The energy level diagram of the Pr^{3+} ion showing the quantum splitting process

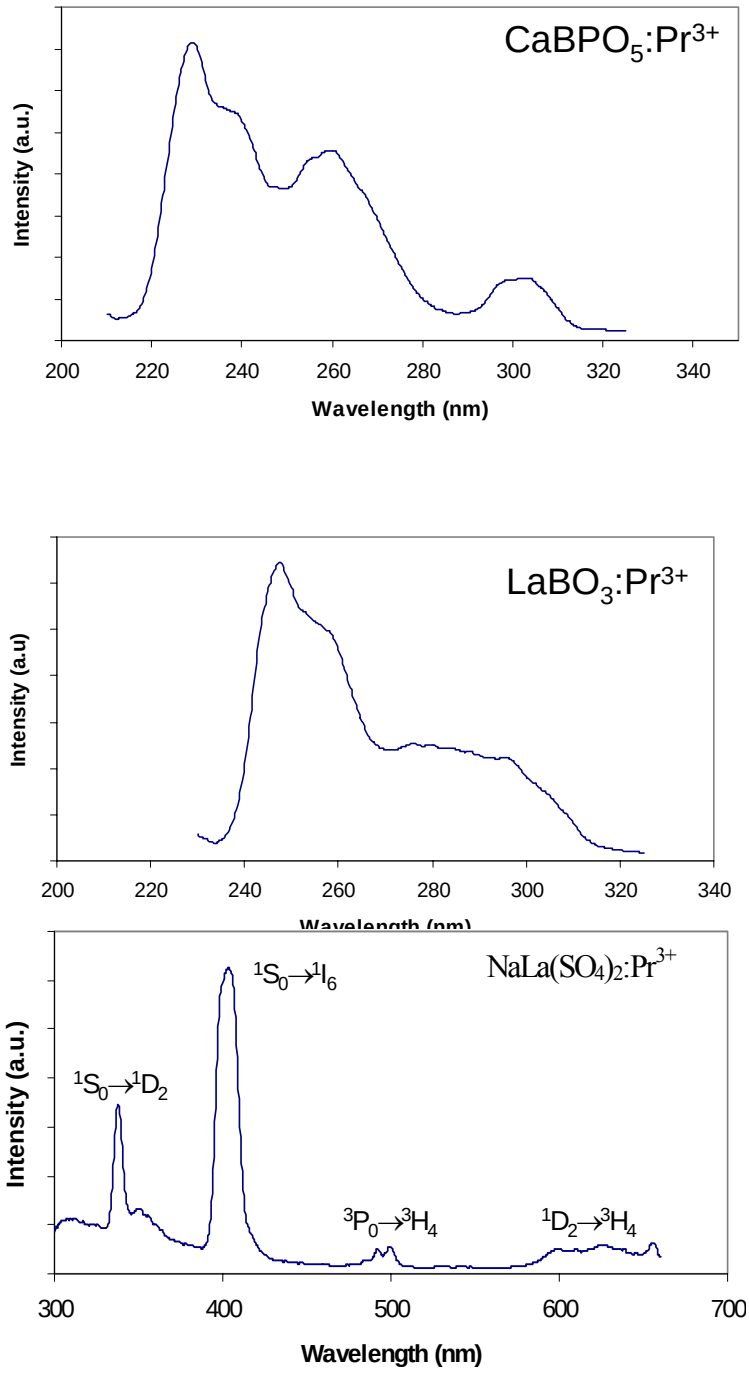

Figure 8. Emission spectra (λ_{ex}=200 nm) some of the new materials discovered in this program.

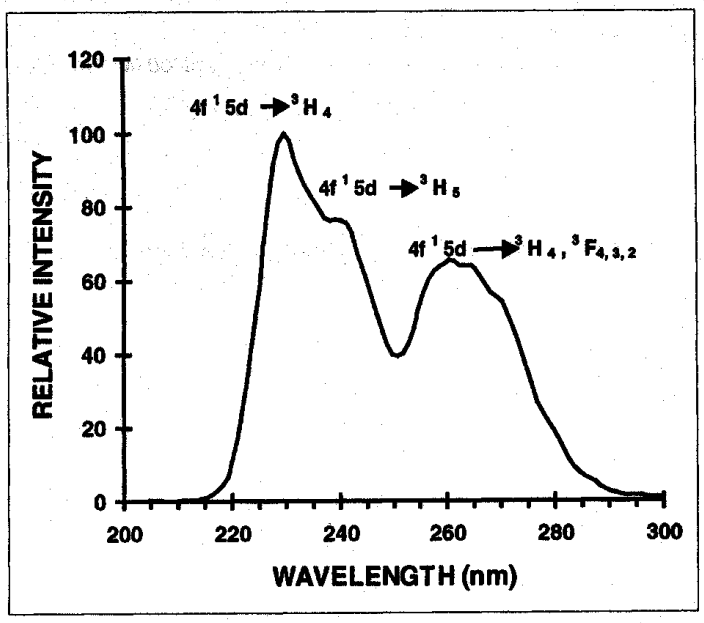

Figure 9: The room temperature emission spectrum of $LaPO_4$: Pr^{3+}

7.3 Synthesis, characterization (physical and optical), and manufacture identified nanophosphors

Since the traditional ceramic approach involving high temperature firing of the well-blended component oxides usually results in large particle size (micrometer) materials, the synthesis of nanocrystalline phosphors requires solution based process and procedures such as colloidal and sol-gel techniques. However, techniques such as flame spray-pyrolysis can also yield nanocystalline phosphors with the desired optical properties. For illustrative purposes we describe the a typical synthesis of some quantum splitting and UV emitting phosphors (the entire process is water based):

Step 1: combine solutions of the desired metal chlorides in deionized water
Step 2: Prepare the surfactant solution (P123, Bicine, PVA, CTAB)
Step 3: Mix the solutions and stir efficiently
Step 4: Raise the pH of the solution to the desired level
Step 4: Dry the precipitate in an oven overnight
Step 5: Calcine at optimum temperature to ensure phase purity.

7.3.1 SAP ($SrAl_{12}O_{19}$:Pr^{3+}, Mg) phosphor

Since the SAP phosphor was down selected for coating on the micron sized phosphor particles, its synthesis and characterization is discussed in considerable details in this section.

A batch of $SrAl_{12}O_{19}$:1% Pr, Mg was prepared by dissolving stoichiometric amounts of $Sr(NO_3)_2$ (Alfa Aesar 99.97%), $Al(NO_3)_3$. $9H_2O$ (Alfa Aesar 99.999%), $Pr(NO_3)_3.6H_2O$ (Alfa Aesar 99.99%), and $Mg(NO_3)_2.6H_2O$ (Alfa Aesar 99.97%), in 100 cm^3 of deionized water under constant stirring for 1 h and subsequent addition of a 5 wt % poly(vinyl alcohol) (Aldrich, 99+% hydrolyzed 115 000 MW) solution. The resulting mixed solution was precipitated by dropwise addition of 100 cm^3 of NH_4OH (28-30%) solution. The obtained material dried in an IR oven for 24 h and calcined at temperatures between 400 and 1400 °C for 4-40 h under air. At each calcination step, a small aliquot of the sample was removed and characterized by X-ray powder diffraction. Microcrystalline $SrAl_{12}O_{19}$:1% Pr, Mg phosphors were synthesized by conventional solid-state reactions of stoichiometric mixtures of $SrCO_3$, Al_2O_3, Pr_6O_{11}, and MgO that were fired between 1300 and 1500 °C under reducing atmospheres.

Upon calcination at 400 °C for 4 h, the $SrAl_{12}O_{19}$:1% Pr, Mg sample showed macroscopically gray areas due to incomplete organic matter decomposition. The sample was subsequently heated at 450, 500, and 550 °C for similar duration and atmosphere. Since macroscopic inhomogeneities still persisted, the sample was removed and milled under 2-propanol using high-density/high-purity Al_2O_3 grinding media for 6 h and subsequently calcined at 600°C for additional 4 h under air. Upon completion of this step, the batch showed no visible grayness and was completely white.

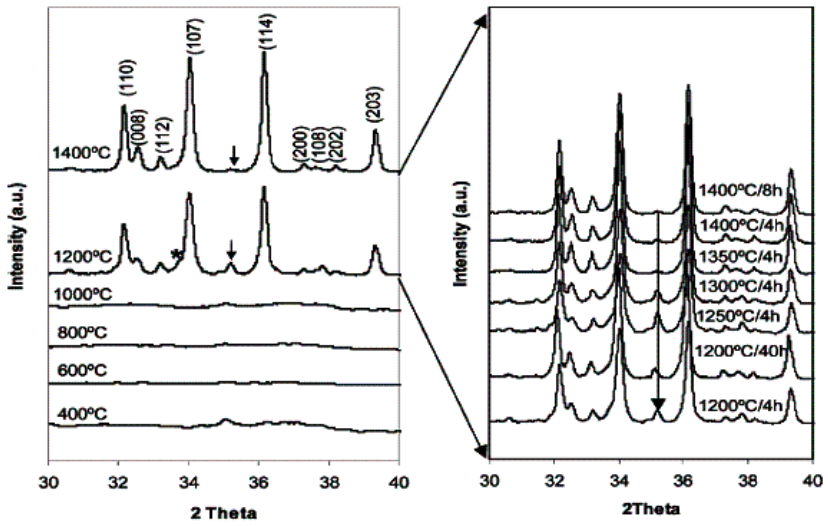

Figure 10: The XRD spectra of $SrAl_{12}O_{19}$:1% Pr, Mg sample synthesized at temperatures between 400 C and 1400 C for 4 hours (left) and at additional calcinations conditions (right). The arrow indicates the reflection of nanosized Al_2O_3. The asterisk indicates unreacted $SrAl_4O_7$.

The X-ray powder diffraction shows absence of reflections belonging to Sr-Al-O phases up to 1000 °C, indicating a mostly amorphous material (Figure 10). At 1200 °C/4 h, the X-ray powder diffraction shows that reflections belonging to the desired $SrAl_{12}O_{19}$:1% Pr, Mg phase are detected. A small amount of unreacted $SrAl_4O_7$ and nanosized Al_2O_3 (signaled by the arrows in Figure 10) still remain in the sample. Increasing the temperature to 1400 °C/4 h considerably increases the proportion of the $SrAl_{12}O_{19}$:1% Pr, Mg phase, and a nearly single phase sample is obtained.

The average crystallite size was carefully verified on samples synthesized under several calcination conditions using both scintillation and position-sensitive detectors and the Scherrer equation (Figure 11). Because of the low dopant levels, no significant lattice strain is expected, and the Scherrer equation provides reasonable crystallite size estimation. It should be noted that the estimate of the crystallite size is volume averaged in the direction perpendicular to the plane of diffraction and therefore provides no information about the nanocrystallite size distribution.

Because of the hexagonal crystal structure, the nanocrystallites tend to adopt anisotropic platelike morphologies. As evidence for anisotropy in the X-ray diffraction patterns, it can be seen that the (114) peak is clearly sharper than the (107) peak, indicating larger sizes in the <110> direction that are found to be outside of the reliable nanoregime that can be estimated using the Scherrer equation. Profile fitting of a (0,0,*l*) reflection would be the preferred choice to estimate the thickness of the crystallites using X-ray diffraction. However, the same platelike nature of the crystallites causes the (0,0,*l*) reflections to be generally weak in intensity (in addition to the fact that they are sometimes convoluted with other reflections). As such, they are less than ideal for crystallite thickness estimation. Thus, the (107) peak was used for size determinations as the <107> direction closely approximates the <001> direction. Taking into account the above-mentioned considerations, we have verified that the different combinations of final calcination temperatures and times yield materials with primary crystallite thickness comprised between ~ 40 and 65 nm (see Figure 10 for samples calcined at different temperatures for 4 h).

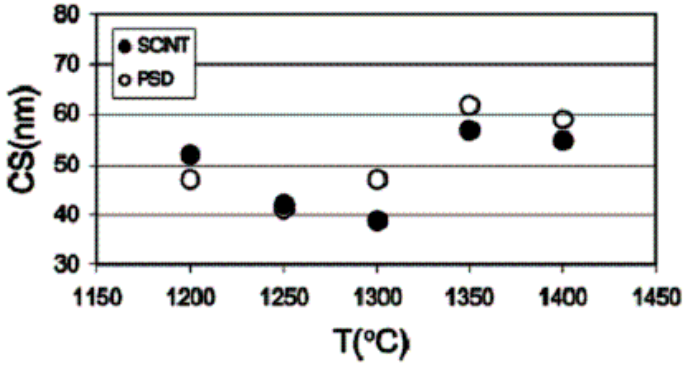

Figure 11: Crystallite size of $SrAl_{12}O_{19}$:1% Pr, Mg phases calined at different temperatures during 4-hour and measured using a scintillation and positron-sensitive detector.

TEM images showed well-defined platelet crystallites with crystallite size in the planar <110> direction ranging from 60 to 300 nm (Figure 12). High-resolution electron microscopy used to assess crystallinity near the particle surface(s) showed no evidence of near-surface amorphization in the $SrAl_{12}O_{19}$:1% Pr, Mg nanocrystallites. Particle thickness was evaluated using the low-loss portion of the energy-loss spectrum to measure the relative intensities of elastic and inelastic scattering. In this technique, absolute particle thickness can be determined from the scattering profile, when the inelastic mean free path (λ_{in}) of a 200-keV electron is known for the material of interest. Although a precise value of ìin is not known for the $SrAl_{12}O_{19}$:1% Pr, Mg phase, we approximate this value as 100-140 nm based on known λ_{in} values for other metal oxide systems. By use of this approach, individual particle thickness is calculated to be 30-35 nm. We have also evaluated the thickness of several agglomerates of $SrAl_{12}O_{19}$:1% Pr, Mg nanocrystallites found stacked together as seen in Figure 5, which vary between ~50 and 80 nm. This correlates well with the XRD values, which indicate a primary crystallite size comprised between ~30 and 60 nm.

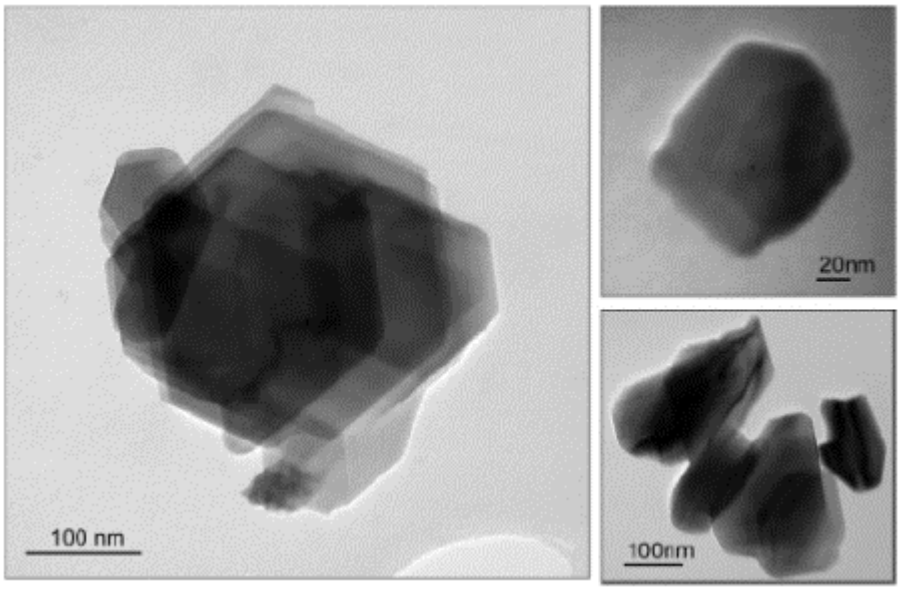

Figure 12: TEM images of well defined platelet nanocrystallites

Figure 13 shows the normalized and corrected luminescence spectra of the nanocrystalline and microcrystalline (insert) $SrAl_{12}O_{19}$:1% Pr, Mg samples at 10 (bottom)

and 290 K (top). A comparison between the emission spectrum for the nanocrystalline sample and that of the microcrystalline material shows that the branching ratios for the $^1S_0$ relaxationat low temperatures and room temperature are statistically identical. The emission lines at 215, 255, 275, 345, and 405 nm are assigned to optical transitions from the $^1S_0$ to the $^3H_4$, $^3F_2$, $^3G_4$, $^1D_2$, and $^1I_6$, respectively. The $^1S_0$ to $^1I_6$ emission and the $^3P_0$ emission at 490 nm constitute the quantum cascade process in this system. A careful comparison shows that the $^1S_0$ to $^1I_6$ transition in the nanocrystalline sample is slightly enhanced, when compared to the microcrystalline sample. The emission spectra not only confirm the preservation of the bulk branching ratio in a 50-nm particle but more importantly demonstrate the absence of impurity or surface induced loss mechanisms which have been reported for other nanocrystalline systems.

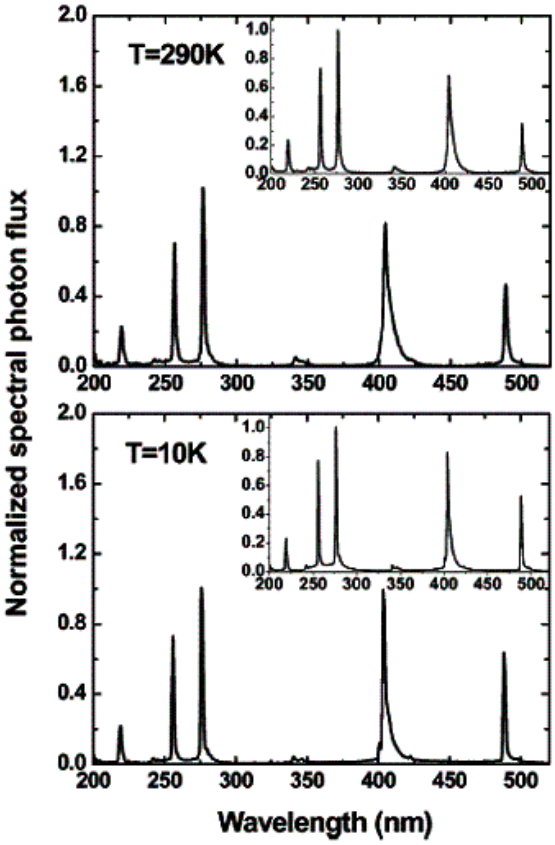

Figure 13: The normalized and corrected luminescence spectra of the nanocrystalline and microcrystalline (insert) $SrAl_{12}O_{19}$:1% Pr, Mg samples at 10 (bottom) and 290 K (top).

We have evaluated the efficiency of our high quality nanocrystalline $SrAl_{12}O_{19}$:1% Pr, Mg by comparing the radiative lifetime of the $^1S_0$ emission in both nanocrystalline and microcrystalline $SrAl_{12}O_{19}$:1% Pr, Mg samples. Figure 14 shows a typical relaxation curve of the $^1S_0$ to $^1I_6$ transition of nanocrystalline sample recorded at 10 K (the detection wavelength is 405 nm). The relaxation can be fit using a single-exponential decay with a relaxation time of 595 ± 5 ns. The relaxation times for the nanocrystalline sample are about 5% shorter than those for the microcrystalline sample. We note that the $^1S_0$ relaxation times are exceptionally fast for a parity-forbidden transition. This is due to mixing with the nearby 4f5d state, leading to relaxation of the parity selection rule.

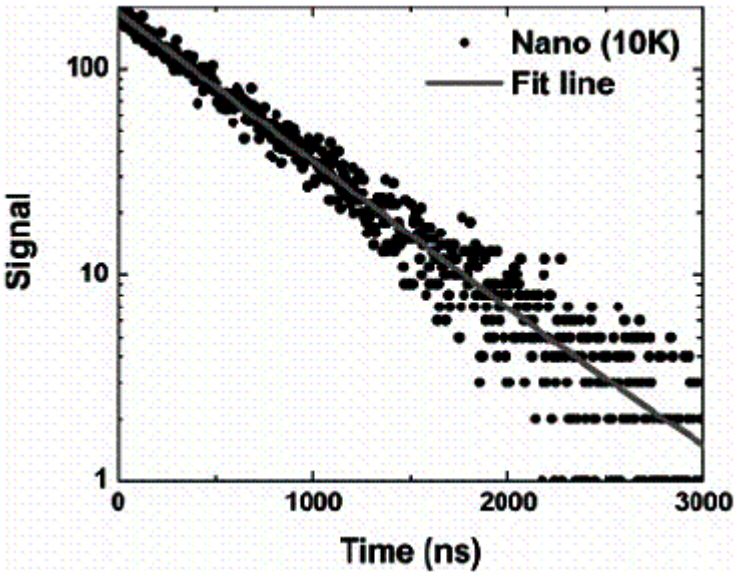

Figure 14: Typical relaxation curve of the $^1S_0$ to $^1I_6$ transition of nanocrystalline sample recorded at 10 K (the detection wavelength is 405 nm).

Figure 15 shows the $^1S_0$ relaxation time as a function of temperature for both samples. The samples show a similar temperature dependence of the relaxation time, i.e., a nearly temperature-independent lifetime at temperature below 200 K, and a weak onset of temperature quenching at higher temperatures. The time-resolved measurements of the nanocrystalline samples show that there are virtually no additional quenching processes in the nanocrystalline samples compared to the bulk samples. In combination with the excitation and emission measurements, this is further evidence of the high quality of these nanoparticles.

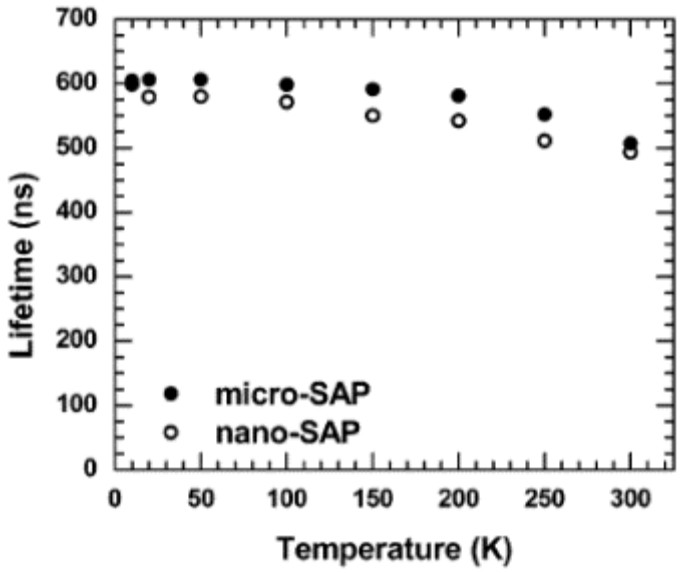

Figure 15: the $^1S_0$ relaxation time as a function of temperature for nano and micron sized $SrAl_{12}O_{19}$:1% Pr, Mg sample.

Figure 16 shows the excitation spectra of the nano- and microcrystalline $SrAl_{12}O_{19}$:1% Pr, Mg at room-temperature normalized to the signal maxima. Once more, we find very similar spectra for the two samples, dominated by the f-d transitions of the Pr^{3+} ion.

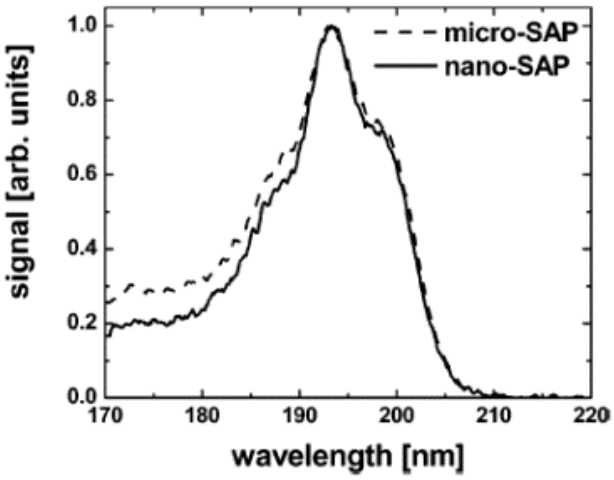

Figure 16: The excitation spectra of the nano- and microcrystalline $SrAl_{12}O_{19}$:1% Pr, Mg at room-temperature normalized to the signal maxima.

Thus, the optical measurements show that no new features in the nanocrystalline phase and the observed small differences from the microcrystalline material are well within the range of variations found in microcrystalline materials synthesized under different conditions. We attribute the fact that the quantum efficiencies displayed by our nanopowders are comparable to those of micrometer-sized powders to two concomitant reasons: the synthesis procedure that yielded high-crystallinity nanopowders that resulted in the absence of additional quenching effects generally observed in other rare earth doped large band gap luminescent nanoparticles; and the rapid relaxation of the praseodymium $^1S_0$ state (~600 ns).

7.3.2 LAP ($LaPO_4:Pr^{3+}$) phosphor

Since the LAP phosphor was down selected for coating on the micron sized phosphor particles, its synthesis and characterization is discussed in considerable details in this section.

In Figure 17 we exhibit the XRD of LAP samples synthesized by using various surfactant. When Bicine and P123 are used as surfactants particles sizes of 14 nm are realized while the use of PVA and CTAB yielded phosphors with 32 nm particle size. However, significant differences in the particle morphology were noted when using the bicine and the P123 surfactants. Figure 18 shows the TEM of the ultraviolet emitting LAP ($LaPO_4:Pr^{3+}$) phosphor produced by two different synthesis routes. Clearly, the morphology and the extent of particle agglomeration is strongly synthesis dependent. The X-ray diffraction analysis (Figure 17) shows that employing different synthesis process can easily produce phosphors with different particle sizes.

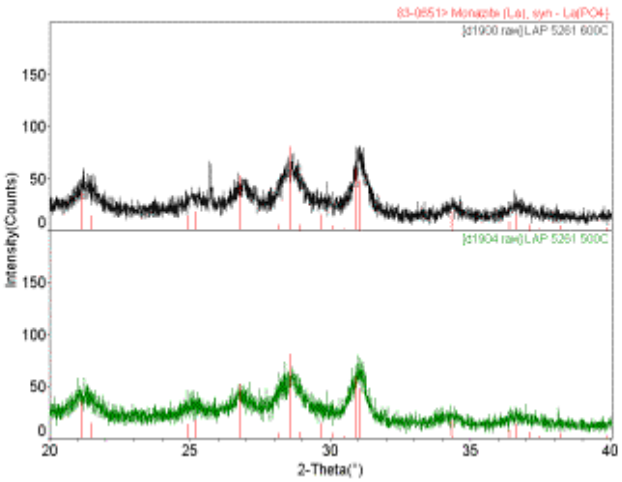

A: Bicine (14 nm)

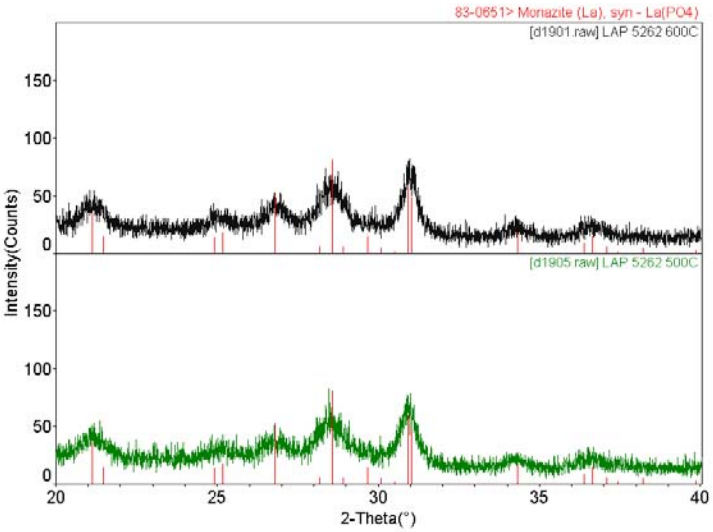

B: P123 (14 nm)

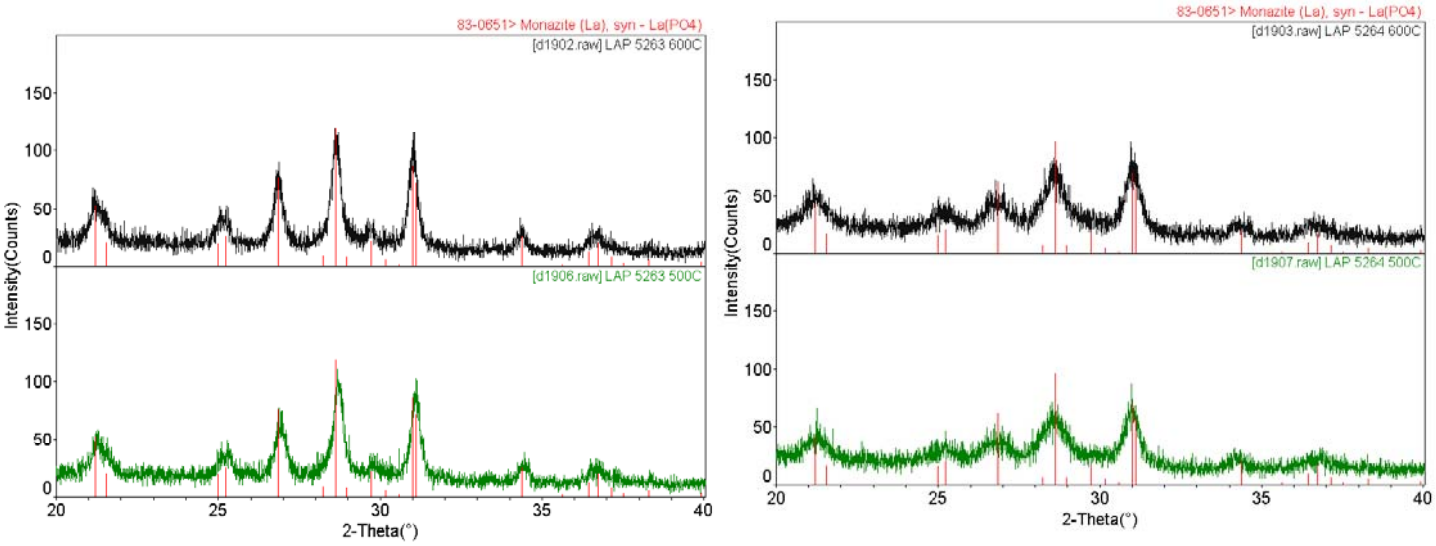

C: PVA 32 nm **D: CTAB 14 nm**

Figure 17: The XRD of LAP samples synthesized by using various surfactant.

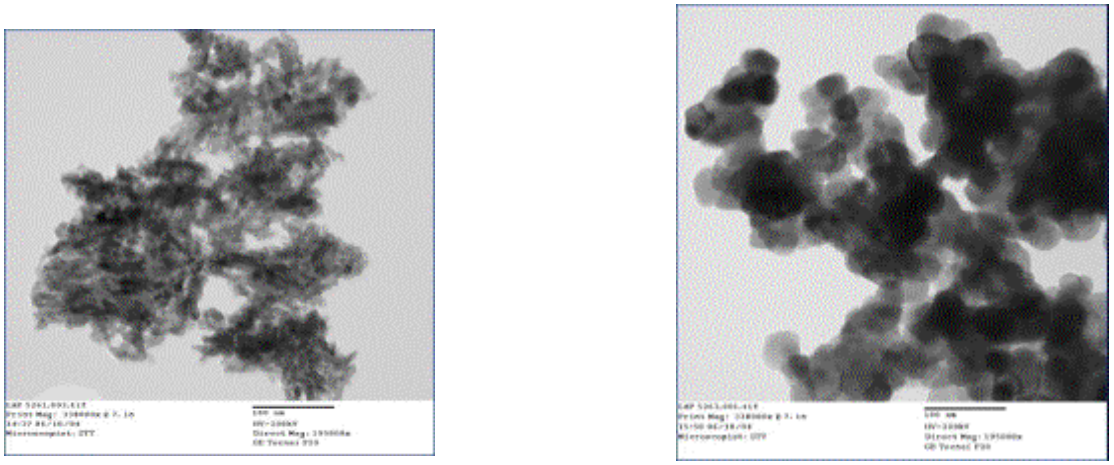

A :Bicine **B : PVA**

Figure 18: The TEM of the ultraviolet emitting LAP ($LaPO_4:Pr^{3+}$) phosphor produced by two different surfactant

The LAP phosphor was also prepared in a unique way, which is described below (Figure 19), by using a carboxylate precursor. The particle size as measured by the line broadening in the XRD was 10 nm, which was confirmed by the TEM images. Unfortunately, the quantum efficiency of the Pr^{3+} emission was found to be quite low in this material.

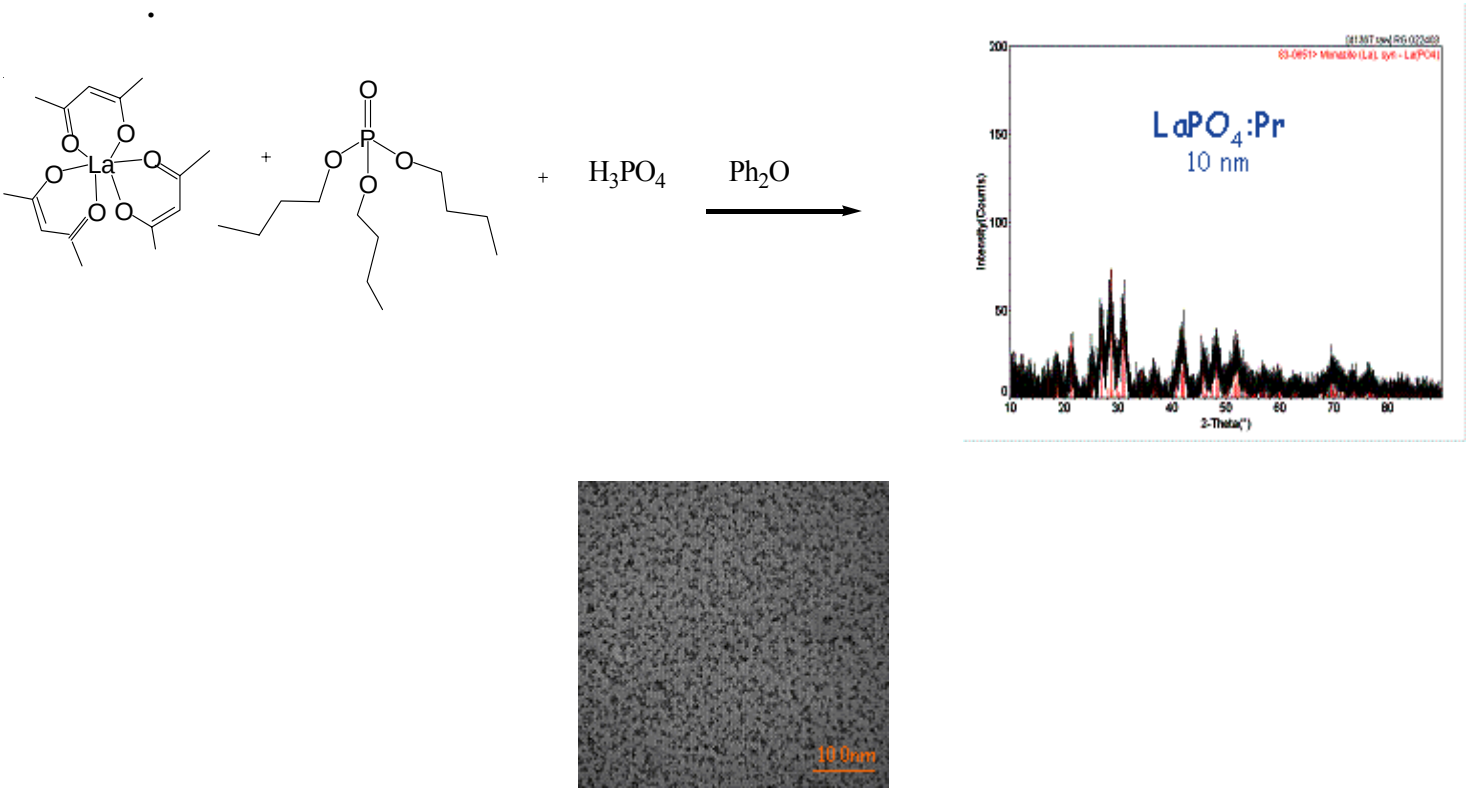

Figure 19 : Synthesis route, XRD and TEM of the 10 nm $LaPO_4$ phosphor particles

Detailed optical characterization of the LAP phosphor is presented in section 7.5.1.

7.3.3 $LaB_3O_6:Pr^{3+}$ phosphor

We now summarize the results of the synthesis and characterization of the quantum splitting phosphor, $LaB_3O_6:Pr^{3+}$. The X-ray diffraction pattern of the nanocrystalline material is shown in Figure 20. The TEM of the particles and the corresponding electron diffraction patterns are shown in Figure 21. The particle size of this phosphor is in the desired range. The X-ray diffraction data for the LaB_3O_6 phosphor prepared by using various templeating agents show that the best sizes is obtained by the Bicine technique (Figure 22). In Figure 23 we show the room temperature emission spectrum of the nanocrystalline borate phosphor. Clearly, quantum splitting is realized in this nanocrystalline material.

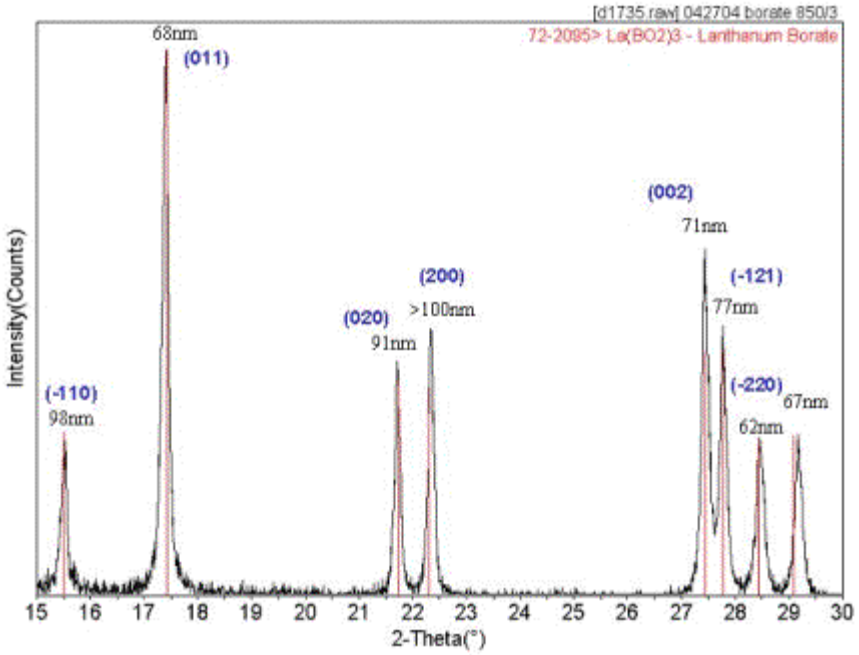

Figure 20: X-ray diffraction patterns of the quantum splitting $LaB_3O_6:Pr^{3+}$ phosphor. The particle size is indicated in the Figure.

Figure 21: The TEM of the quantum splitting $LaB_3O_6:Pr^{3+}$ phosphor.

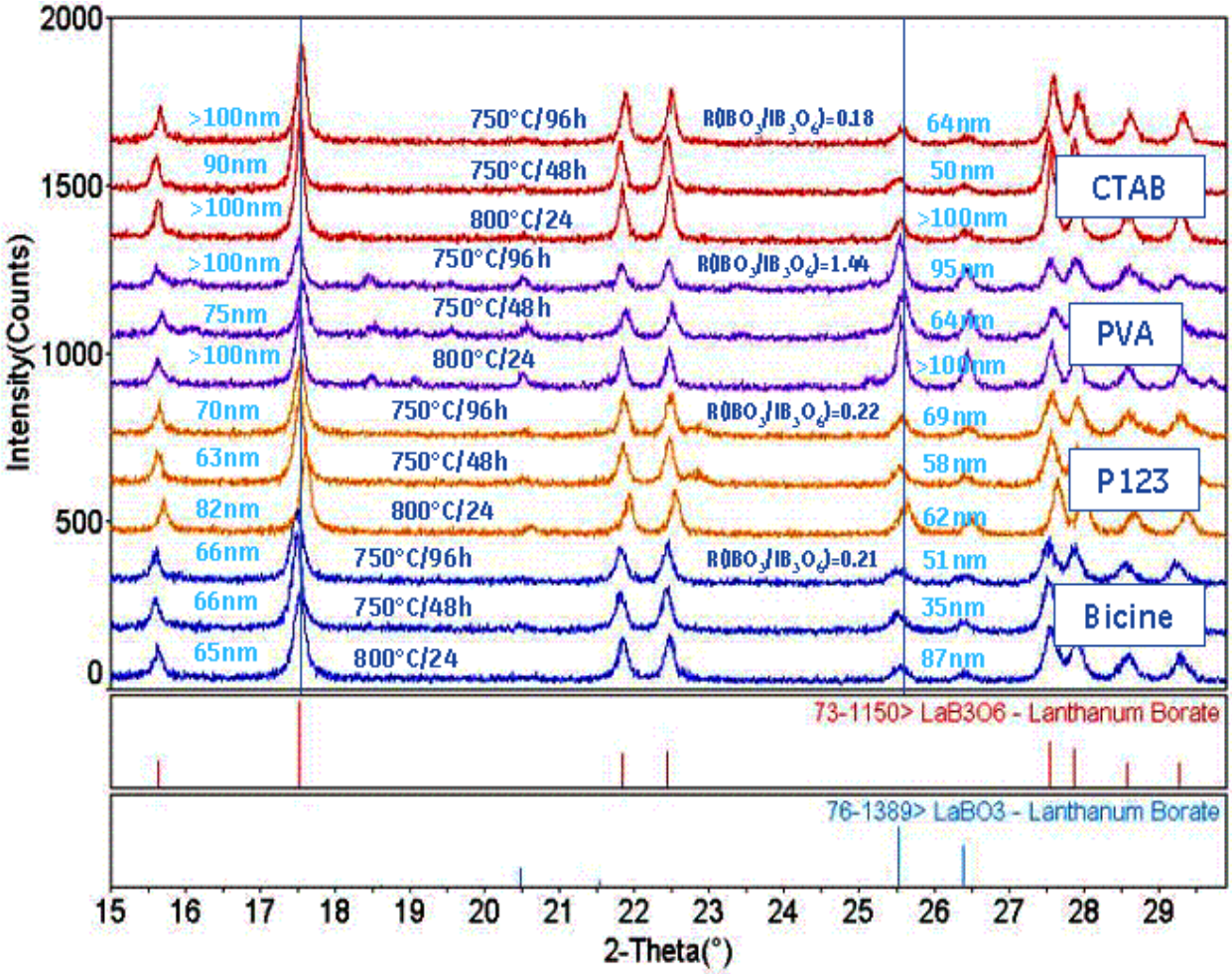

Figure 22: The XRD of LaB_3O_6 samples synthesized by using various surfactant. The particle sizes are indicated in the figure.

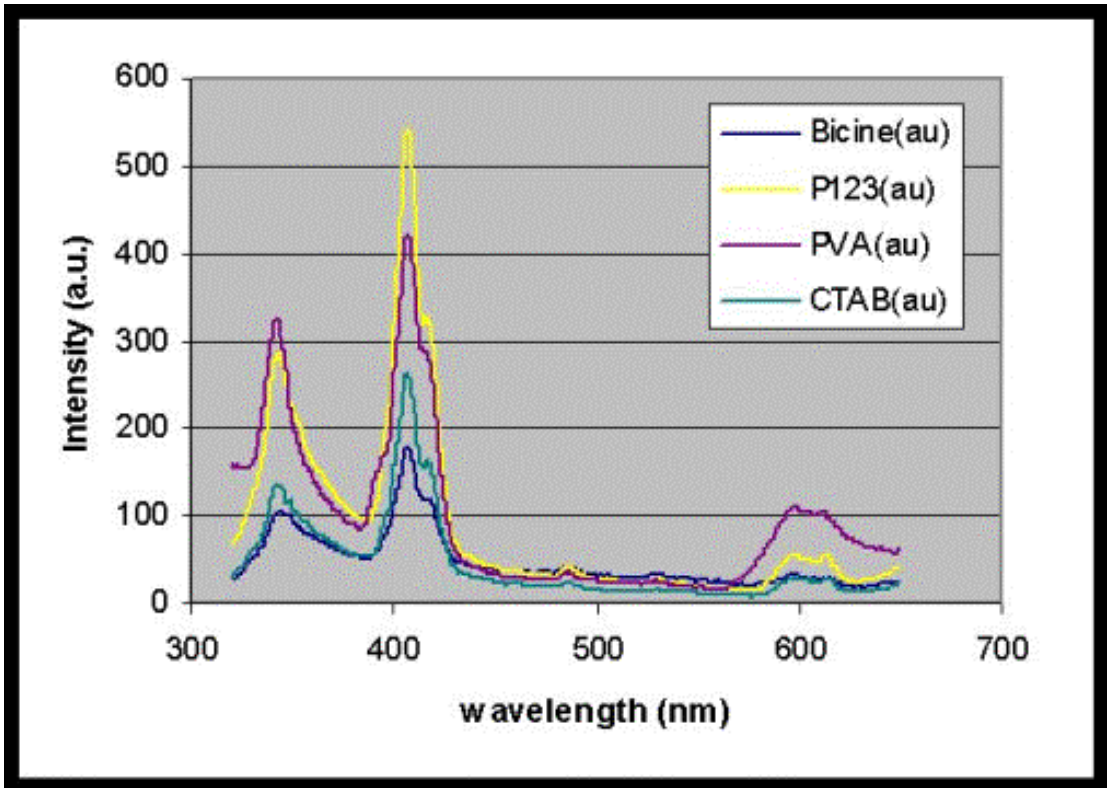

Figure 23: The room temperature emission spectrum of the nanocrystalline Quantum splitting phosphor $LaB_3O_6:Pr^{3+}$

7.4 Coating of core phosphor particles by nanosized phosphors

7.4.1 Solution techniques

The attainment of uniform coating of the nano phosphors over the micron sized phosphor particles is the major task to which we devoted the vast majority of our technical development effort. The focus for development work along the prime technical path was the trivalent praseodymium ion in an previously identified host lattice. It is noteworthy that the successful attainment of a uniform coating over the core particles requires the determination of optimum conditions of synthesis, which is usually a lengthy task because there are many independent parameters, such as (1) the temperature of precipitation (2) the rate of precipitation (3) the ratio of the reactants (4) the atmosphere and the temperature-time cycle during reaction. The attainment of a successful coating requires that a large number of samples be synthesized and tested for their quantum efficiency and absorption of 254 nm UV radiation. In this section we provide an overview of progress made in developing (synthesizing) coated "hybrid" phosphors.

Essentially the coating experiments were carried out by precipitating the nano phosphors on to the surface of the commercially available phosphors. For coating purposes, it is essential to determine the morphology of the nano particles and their state of aggregation. This is strongly dependent on the synthesis procedure. As an example, in Figure 24, we show the electron micrographs of a particular nano phosphor (LAP) that have been synthesized in two different ways. It is quite evident that in the two different synthesis procedures results in different degree of particle aggregation. Particles in the electron micrograph shown on the left hand side are highly aggregated while particles on the right hand side are well dispersed. It is also evident that the morphology of the particles is that of the needle type.

Figure 24: SEM of nano particles synthesized under two different conditions. The particles on the left are highly aggregated and particles on the right are well dispersed. Note the needle like morphology of the particles.

From both the physical and chemical standpoints, the role of the interacting surfaces between the nano particles and the core particles is of considerable importance. It should be noted that the coating process may be essentially physical in nature or it may result in chemical bonding between the nano and the core particles. If the coating is physical in nature then one must consider the electrostatic interaction between the surfaces of the particles. Hence knowledge of the Zeta potential of both the core and the nano particles is of great importance. We employed Zeta potential measurements to understand the nature of bonding between the nanoparticles and the core phosphor particles. As an example, in Figure 25 we exhibit the zeta potential of the core particle and that of the nano phosphor particles as a function of the solution pH.

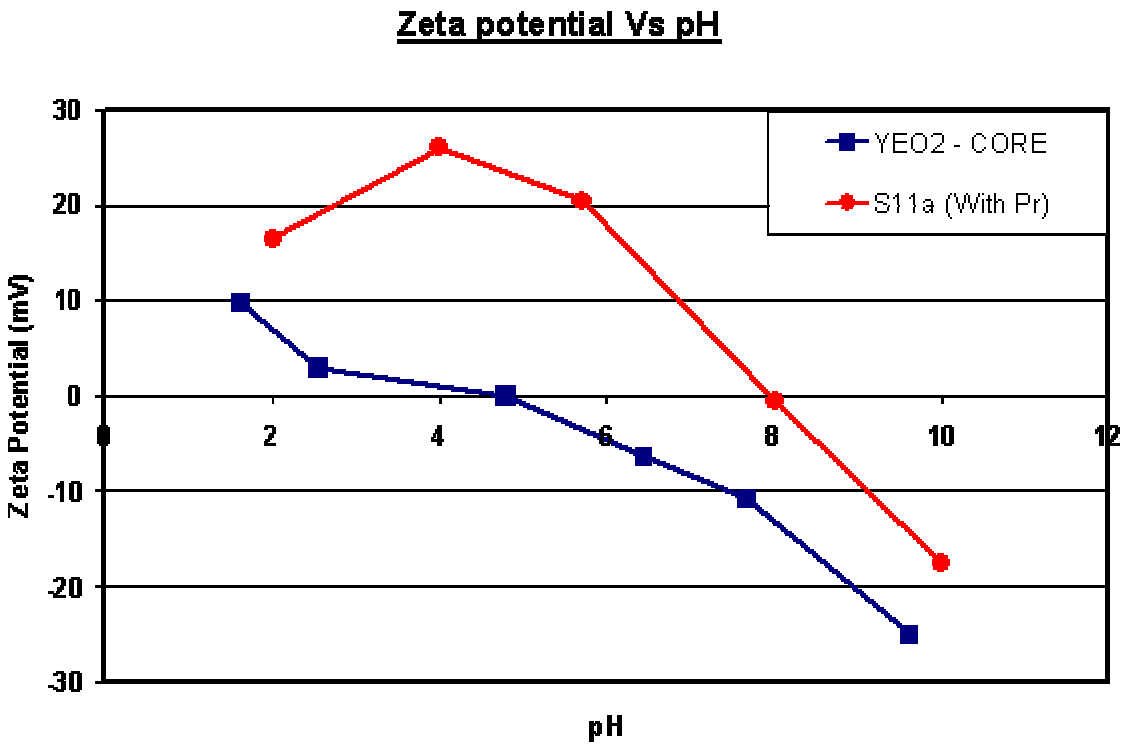

Figure 25: Zeta potential values over a range of pH for the core particle and the nano phosphor particles.

The results from the Zeta potential measurements and as exhibited in figure 25, showed that for this specific system the optimum condition for the coating experiments is at a solution pH of 6. We used both the aggregated and the well-dispersed nano particles in the coating experiments to evaluate the differences in the relative coating efficiencies. Figure 26a shows that with the well-dispersed particles a more uniform coating is attained relative to the agglomerated precursor material where the coating is rather very irregular (Figure 26b).

(a) (b)

Figure 26: Transmission electron micrograph of coated particles (a) well-dispersed precursor and (b) aggregated precursor.

The surface coating so obtained and as evidenced from the TEM of Figure 26 is very thin. The thickness of the coating layer was found to be dependent on the precipitation rate. Fast precipitation rate, which occurred when the reactants were mixed usually, gave very thin surface layer. Hence, by controlling the precipitation rate it should be possible to control the thickness of the coating layer. This involved a rather extensive study of the main interactions between the various synthesis parameters such as reactant concentration, flow rate and temperature, to name a few. The end result of this study was the development of a new controlled precipitation technique that yielded uniform and thick surface layer of the nano particles on the core particles.

The TEM of the final product obtained from the optimized proportions and method of precipitation is shown in Figure 27. It should be noted that complete covering was observed on all the particles. In general, if the samples were prepared at room temperature, the coating thickness varied from 100 to 150 nm while for samples prepared at elevated temperatures (80 C), the thickness varied from 100 nm to 200 nm. The entire coating process was completed during the first thirty minutes. Longer times did not result in thicker coating.

In order to further increase the coating thickness an attempt was made to repeat the above coating process onto a core particle that was already coated. The repetition yielded a uniform multiple nano bilayer coating on the core phosphor particles. Figure 28 shows that the coating thickness could now be increased to 200-300 nm.

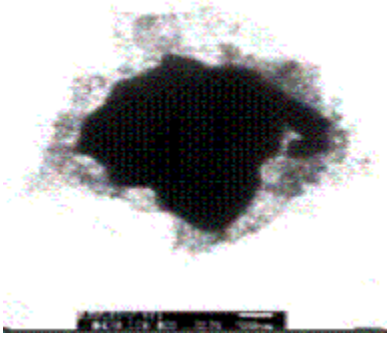

Figure 27: Transmission electron micrograph of coated particles using well-dispersed precursor.

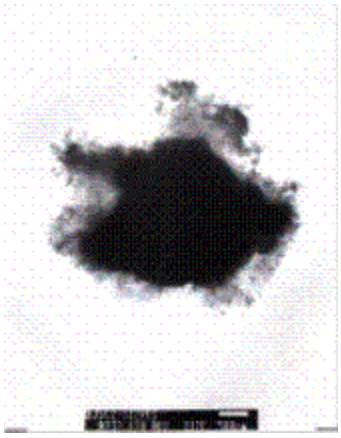

Figure 28: Transmission electron micrograph of double coated particles using well-dispersed precursor.

In the above experiments the morphology of the precursor nano particles are characterized by thin needle like structure. Although there is not a comprehensive set of data on which to base a broad statement, it seems that there may be some limitations to the extent to which the thin needle like materials may uniformly coat the core particles in an efficient manner. It is for this reason that we also investigated the coating efficiency with nano particles that are thicker and more elongated than the needle like materials.

The TEM of thicker and elongated precursor particles produced using the surfactant techniques developed within the program is shown in Figure 29. The particle size of the precursor was measured by the technique of X-ray diffraction and determined to be approximately 32 nm (Figure 30). The TEM of the coated particles using such precursor particles is exhibited in Figure 31. It is observed that a uniform and relatively strong outer coating is attained.

The quantum efficiency and the intrinsic ultra-violet (254 nm) absorption of the core particles after the coating process remained high and similar to that of the uncoated particles. This shows that the outer coating by the nano particles did not adversely influence the 254 nm reflectance. We were also successful in producing a large batch (85 grams) of the coated particles by the surfactant technique.

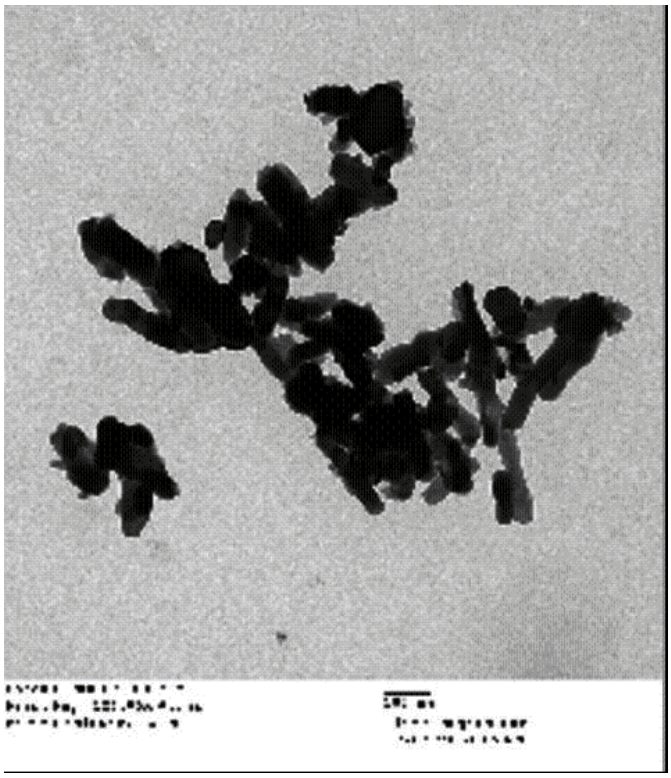

Figure 29: Transmission electron micrograph of precursor particles synthesized by a propriety technique.

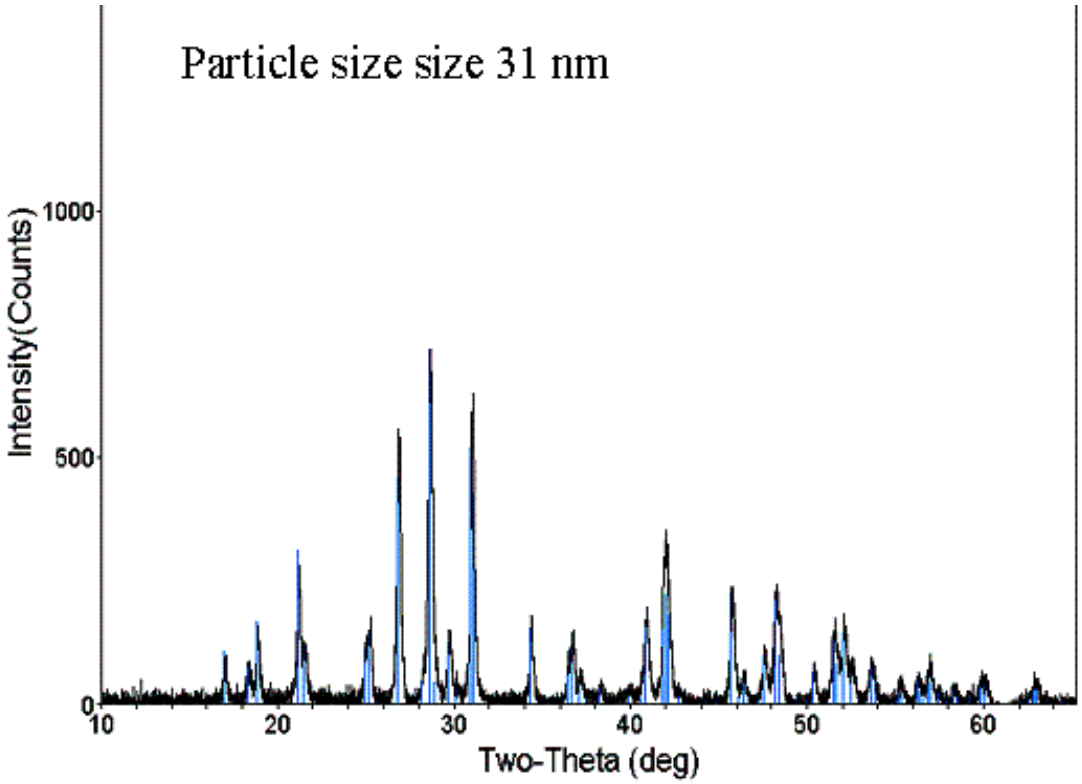

Figure 30: The X-ray diffraction pattern of the precursor material showing the attainment of particles with 31 nm particle size.

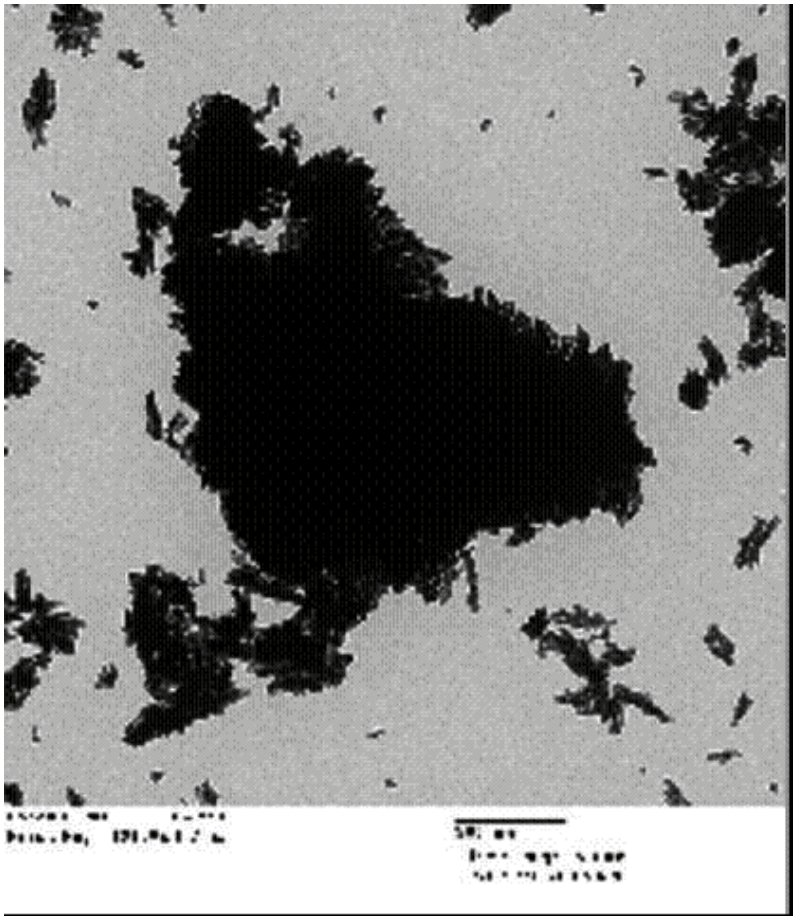

Figure 31: Transmission electron micrograph of coated core particles

Experiments on coatings of nano-sized LAP:Pr on YEO, and LAP:Pr on LAP:Ce, Tb have been carried out using several different methods, including in-situ coating, and ex-situ coating technical approaches (Fig. 32-top, and bottom, respectively).

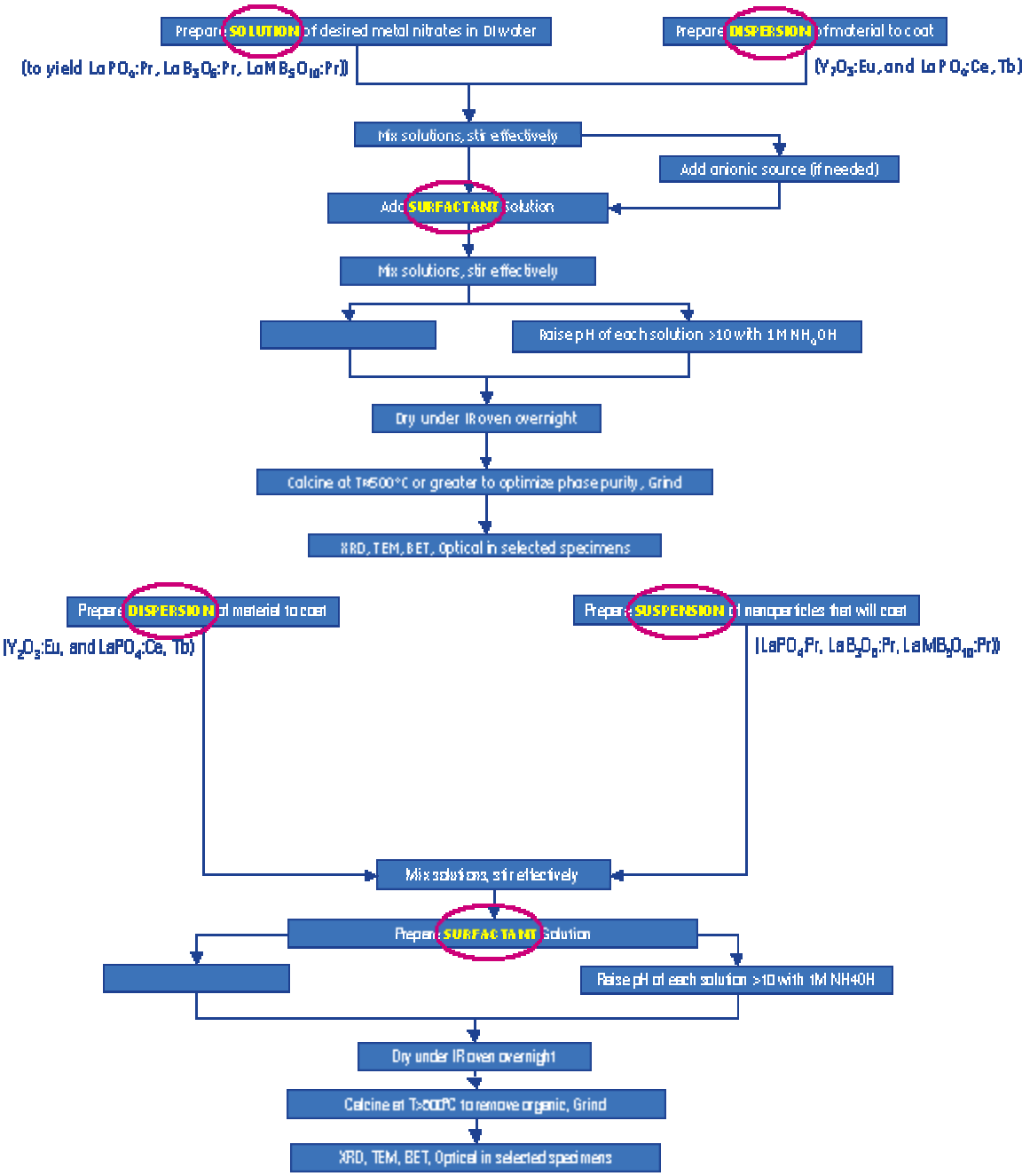

Figure 32: Schematic experimental procedure for in-situ coating technical approach (Top), and ex-situ coating technical approach (Bottom)

Figure 33 shows that an in-situ procedure for a $LaPO_4$:Pr coating on Y_2O_3:Eu using surfactants with high ionic strength (such as CTAB) leads to marginally effective coating with low surface coverage. In addition, yttrium and europium from the Y_2O_3:Eu micron size particles, leaches into the solution and is incorporated into the $LaPO_4$:Ce,Tb structure, yielding a (La,Y)PO_4:Ce, Tb, Eu mixed phase. This results in very low QE for the hybrid system (~ 20%).

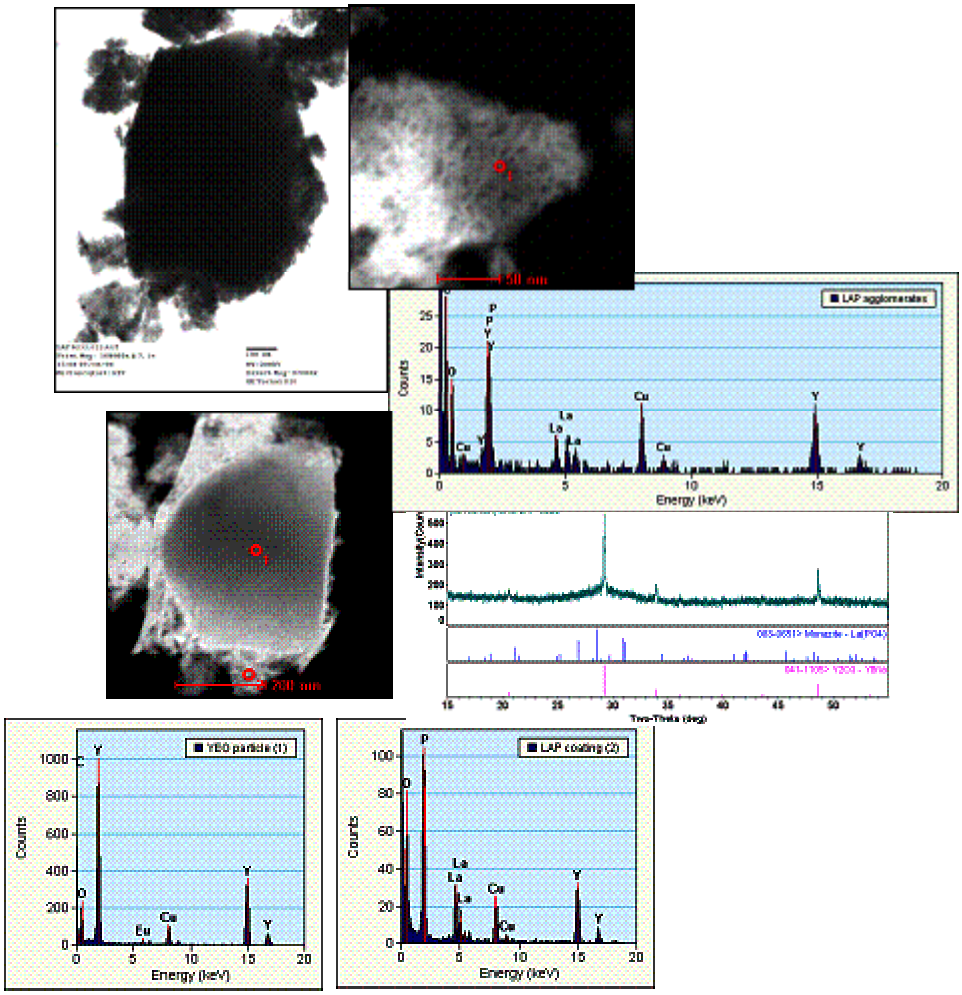

Figure 33: X-ray diffraction, transmission electron microscopy, and energy dispersive spectroscopy analysis for samples of $LaPO_4$:Pr coated onto Y_2O_3:Eu micron size particles using an ex-situ coating technical approach.

Extensive screening experiments on these and modifications on the technical coating approaches with the goal of optimizing QE of the hybrid system have been carried out within the program. The experiments took into account both in-situ and ex-situ coating procedures and variation of several processing factors such as chemical nature of the surfactant, ratio between surfactant and reactants yielding the nano-QSP, ratio between nano-QSP coating and micron size phosphor, and final temperature and calcination times. The lamp test results of the final coated hybrid phosphors developed by using the above described techniques will be discussed in section 7.6.

7.4.2 Coating of phosphors by flame pyrolysis

In this section we describe a continuous powder synthesis by flame processing based on the PVA method. In Figure 34, we show the schematic drawing of the small, pilot –plant scale for the production of fine ceramics.

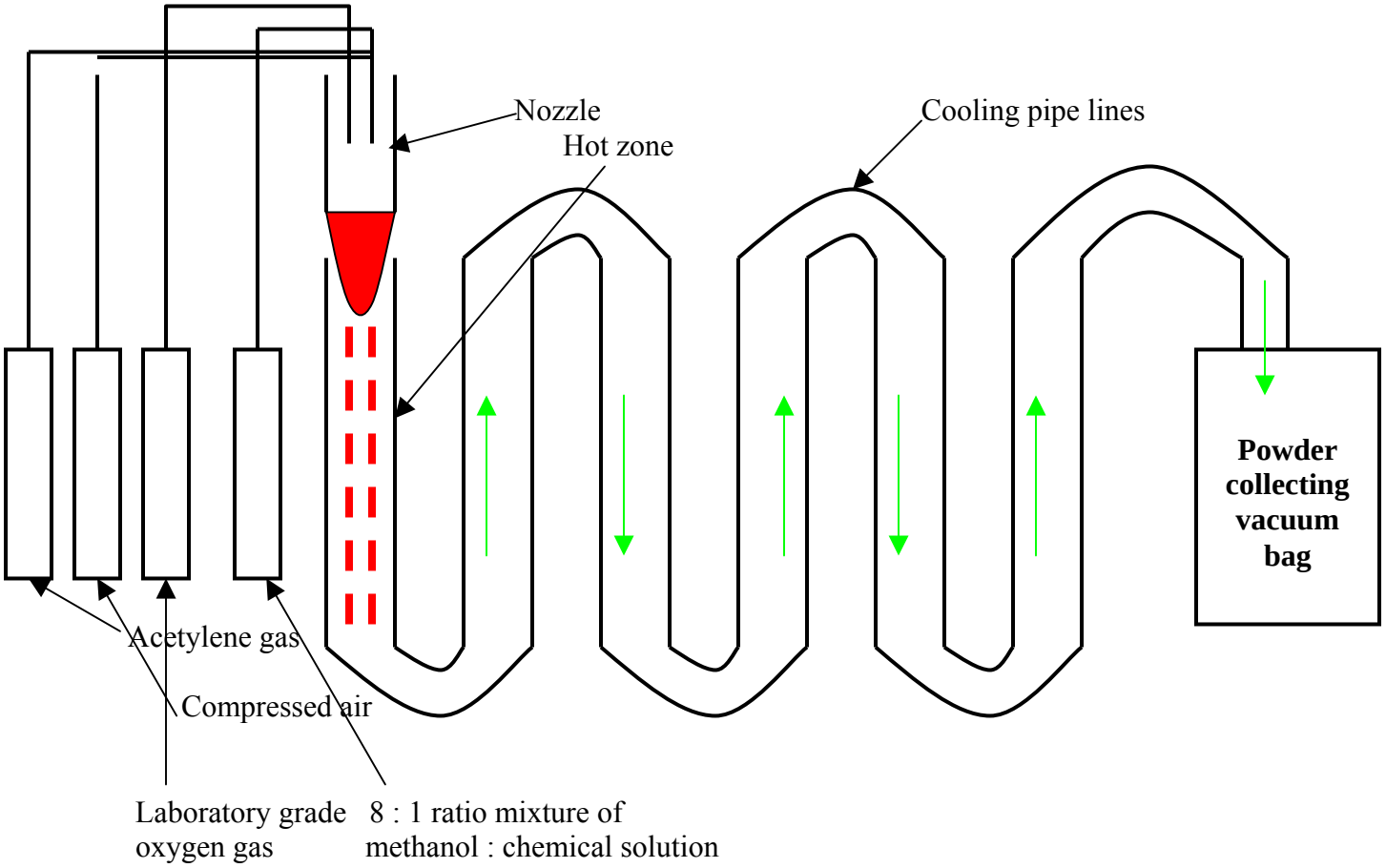

Figure 34. Schematic drawing of the small, pilot-plant scale, production line of fine ceramic powderd. (Green arrows indicate the flow of powders in the production line).

Considerable effort has been spent to produce fine ceramic powders such as $La_{0.99}Pr_{0.01}PO_4$ coated YEO (Y_2O_3:Eu) powder by using the continuous powder production facility shown in Fig. 34. As an example, with the 20g batch of spinel composition in solution, about 13g of final powder was collected in the vacuum bag giving a yield of higher than 65%. PVA (polyvinyl alcohol, molecular weight : 9500, Aldrich Chemical Inc.) was used as polymeric source.

The coating of $La_{0.99}Pr_{0.01}PO_4$ coated YEO (Y_2O_3 : Eu) powder

Lanthanium nitrate hexahydrate [$La(NO_3)_3 \bullet 6H_2O$, Aldrich Chemical. Inc.], praseodymium (III) nitrate hexahydrate [$Pr(NO_3)_3 \bullet 6H_2O$, Aldrich Chemical Inc.] and boric acid [H_3BO_3, Aldrich Chemical Inc.] were used as La^{3+}, Pr^{3+}, and B^{3+} chemical source, respectively. The polymeric ratio of PVA used was 16:1. The final chemical solution was diluted by methanol with 8 times larger volume. The mixture of chemical solution and methanol was finally sprayed into hot zone.

As-received YEO powders showed faceted surfaces with some kinds of particles on the surfaces, as shown in Fig. 35.

Figure 35 : SEM pictures of as-received YEO particles (commercial phosphor)

The amount of $La_{0.99}Pr_{0.01}PO_4$ on each YEO particle was intended to make a coating with 50 nm thickness on the individual YEO particle by using 0.0682 weight ratio of $La_{0.99}Pr_{0.01}PO_4$ to YEO (Y_2O_3 : Eu) powder. Fig 36 is the XRD profile of coated YEO powders. All the major peaks matched well with Y_2O_3 standard peaks.

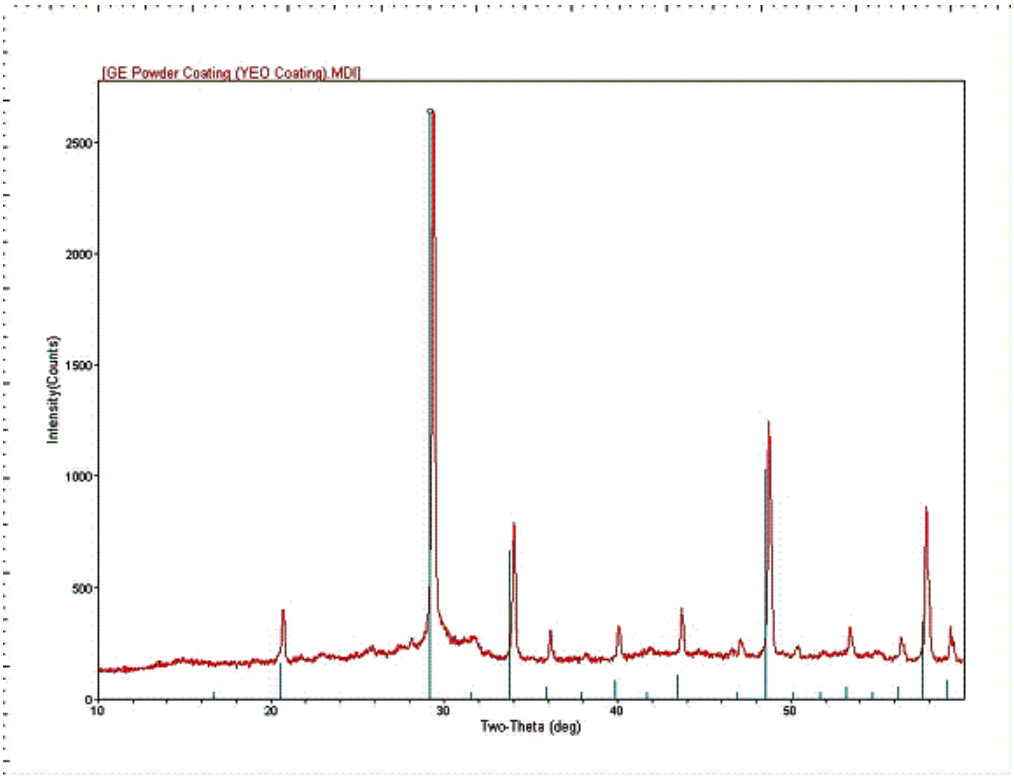

Fig. 36 XRD profile of YEO powders coated with $La_{0.99}Pr_{0.01}PO_4$ particles fabricated by flame processing based on the PVA method.

The BET specific surface area of as-synthesized YEO powder coated with $La_{0.99}Pr_{0.01}PO_4$ was 8.8242 m^2/g.

SEM micrographs of YEO powders coated with $La_{0.99}Pr_{0.01}PO_4$ are shown in Fig. 37. Even though micrographs indicated relatively homogeneous coating of $La_{0.99}Pr_{0.01}PO_4$ on YEO particles, the amount of coating was assumed relatively too much. Therefore, little less amount of coating would be necessary.

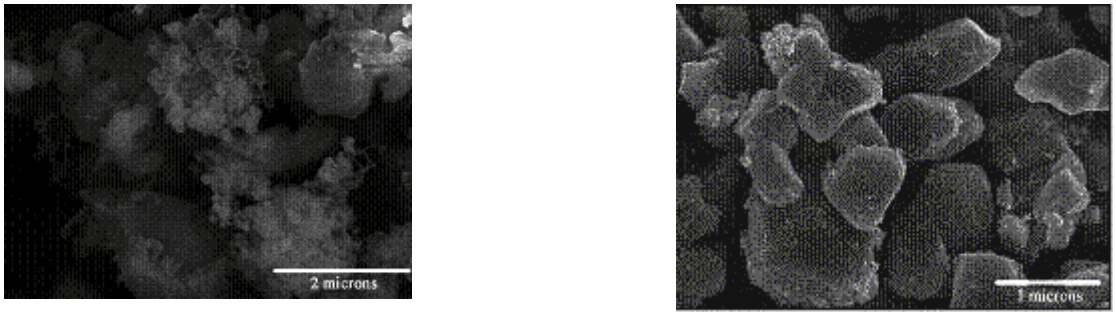

Fig. 37. SEM micrographs of YEO powders coated with $La_{0.99}Pr_{0.01}PO_4$ particles fabricated by flame processing based on the PVA method.

YEO (Y_2O_3 : Eu) powder coated with reduced amounts of $La_{0.99}Pr_{0.01}PO_4$

Reduced amounts, by half, of $La_{0.99}Pr_{0.01}PO_4$ was used to coat YEO particles and this coating formulation indicated better homogeneous coating of $La_{0.99}Pr_{0.01}PO$ particles without the presence of too much excess as shown in Fig. 38. The SEM pictures shows necking formation indicating complete coating of $La_{0.99}Pr_{0.01}PO_4$ on the surface of YEO powders.

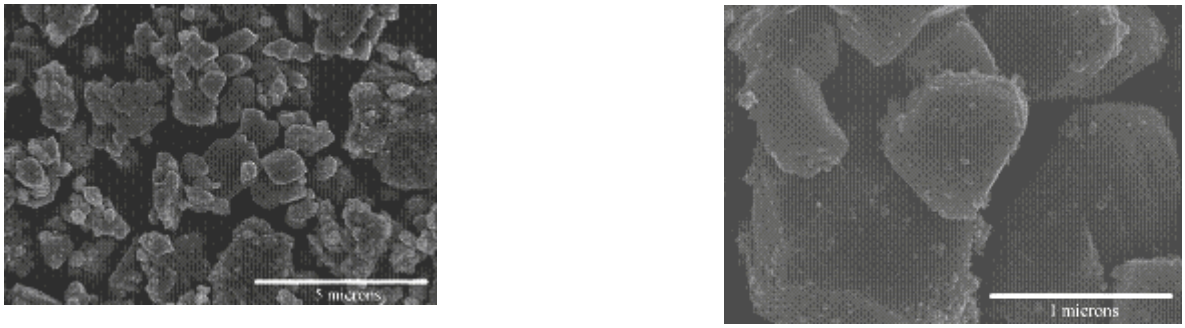

Figure 38. SEM micrographs of YEO powders coated with half amounts of $La_{.99}Pr_{0.01}PO_4$ particles compared to those shown in Fig. 37.

7.4.3 Plasma Method to produce nano particles of SAP and LAMB

Our goal is to coat YEO (yttrium oxide doped with europium) with SAP (strontium aluminate doped with praseodymium). Previous experiments of trying to coat YEO with SAP by a sol-gel process were unsuccessful, so a new route of synthesizing SAP on YEO is needed. The current method being explored is to synthesize SAP using a RF plasma. This is accomplished by feeding an aqueous salt solution containing aluminum chloride hydrate, strontium nitrate, and praseodymium nitrate hydrate through the RF plasma and collecting the powder. The plasma torch assemble is shown in Figure 39.

Figure 40 shows the plasma conditions for two reactions using the same solution concentrations. Experiment tt087 was successful in producing SAP but the powder was retained inside the plasma torch housing instead of exiting as desired. The synthesis conditions varied in initial molar concentrations of the salts as well as ratios of Al to Sr salts and gas flows in the torch.

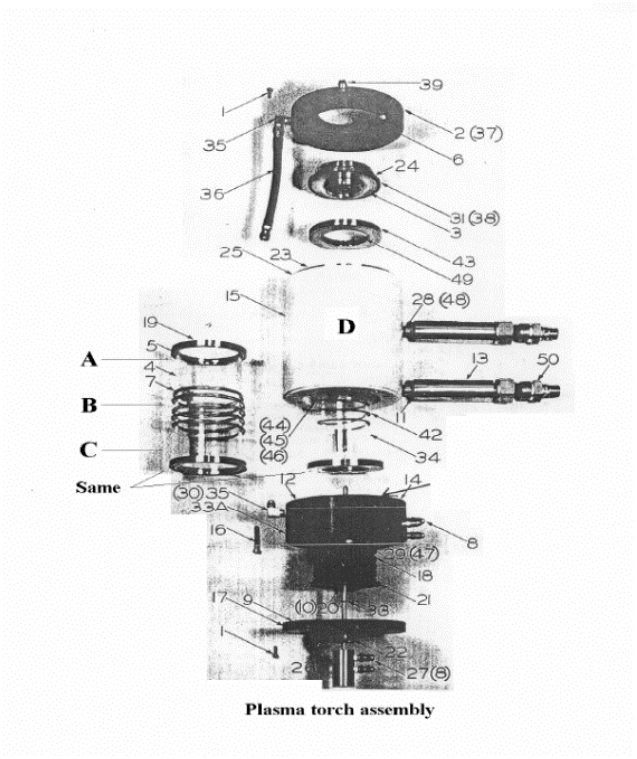

Figure 39: The plasma torch assembly

ID	tt087	A-6
swirl rate	7.5%	7.5%
axial rate	0.0%	10.0%
radial rate	2.5%	2.5%
O_2 rate	0.5L/min	0.5L/min
power	20%	20%
nozzle	old	new

Figure 40: Experimental condition for the synthesis of SAP samples

XRD showed that experiment tt087 produced $SrAl_{12}O_{19}$ and Al_2O_3 in regions A and C of the torch assembly. By increasing the axial flow rate and increasing the inner diameter (ID) of the front nozzle (Part #24) in experiment A-6, powder was collected in region A of the torch assembly. The change in flow rate and ID of the front nozzle was done in an attempt to find conditions to push the powder out the plasma torch so YEO could be coated in the cooler region. Unfortunately, the powder that was collected was amorphous (by XRD). It is assumed that the increased axial flow circulated the droplets and/or the mixed salt particles after water evaporation too quickly through the plasma, which prevented thermally induced solid-state reaction to produce the desired SAP.

LAMB ($LaMgB_5O_{10}:Pr^{3+}$) plasma experiments

Like the SAP, our goal is to coat YEO with lanthanum magnesium borate (LAMB). Previous sol-gel methods formed the correct LAMB compound with the crystallite size less than 100nm, but the compound was a grey color. By using plasma synthesis, we hope to obtain a white powder with a crystallite size less than 100nm.

Experimental

Boric acid, lanthanum chloride, magnesium chloride and praseodymium nitrate were dissolved in water. The solution was sonicated into a mist and fed through the plasma. The plasma conditions are shown in Figure 41.

ID	A-7
swirl rate	7.5%
axial rate	5.0%
radial rate	2.5%
O_2 rate	0.5L/min
power	20%
nozzle	old

Figure 41: Experimental condition for the synthesis of LAMB samples

The powder was collected in region A on the torch assembly, but the powder only contained lanthanum, magnesium, and oxygen (by SEM/EDS). We first concluded that the results suggest that the boric acid is sublimed from the solid particles remaining after water evaporation, leaving only the mixture of lanthanum and magnesium oxides. However, in a separate SEM/EDS evaluation of an authentic mixture containing boric acid, or a sample of only boric oxide, boron was not identified.

7.4.4 Summary of the results obtained from Nanocerox precursors

We briefly summarize the optical characterization work performed on the quantum splitting SAP samples that were synthesized by Nanocerox by their propriety method. Essentially the technique consists of introducing the precursors in a hot combustion chamber where the reaction occurs and trapping the so formed nano powders in the collector (Figure 42).

The precursor samples received from Nanocerox were subjected to various heat treatment processes to attain the desired crystalline phase while maintaining the phosphor particle size in the 100 nm range. The room temperature emission spectra of the as- received sample and the heat-treated samples are shown in Figure 43. The X-ray diffraction pattern indicated single-phase formation when the samples were heated at 1200 C. The estimated particle size of this material was 49 nm (Figure 44). We note here the demonstration of quantum splitting in this material. Nanocerox has also synthesized the corresponding $CaAl_{12}O_{19}:Pr^{3+}$ phosphor and our optical investigations have clearly demonstrated the occurrence of quantum splitting in this material. The results obtained from the Nanocerox precursors are very encouraging since the work demonstrates potential manufacturing technique of these nanocrystalline phosphors.

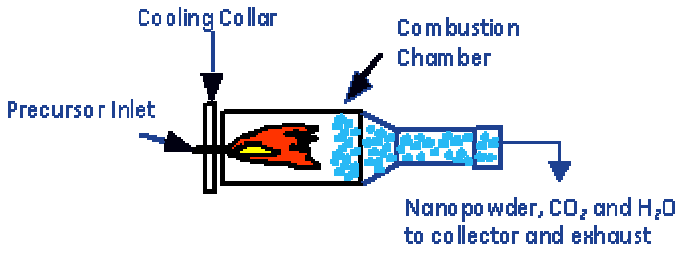

Figure 42: Schematic of the reaction assembly to produce nano particles

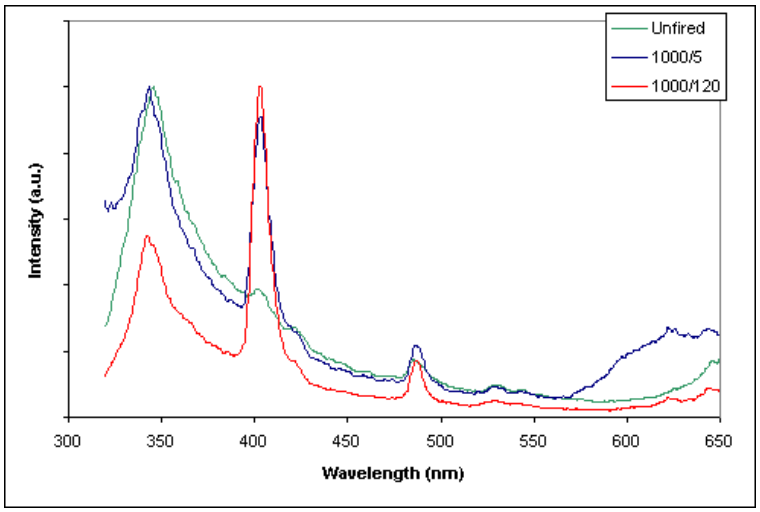

Figure 43: The room temperature emission spectrum of the Quantum splitting phosphor $SrAl_{12}O_{19}:Pr^{3+}$ phosphor from precursors obtained from TAL Materials, Inc. (green: as-obtained material; blue: fired at 1000C for five hours; red: fired at 1000 C for 120 hours).

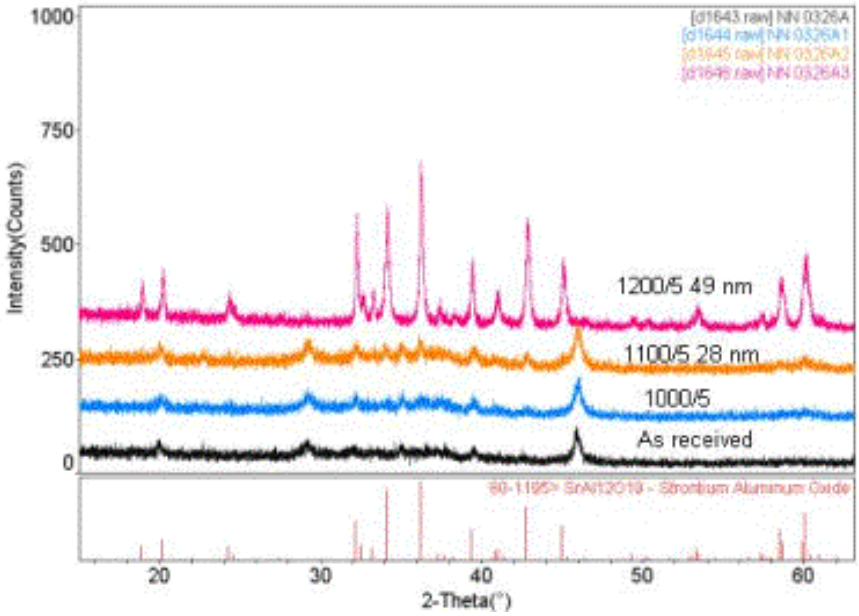

Figure 44: X-ray diffraction patterns of the quantum splitting $SrAl_{12}O_{19}:Pr^{3+}$ phosphor from precursors obtained from TAL Materials, Inc. The precursors were heated to various temperatures/time. The particle size is indicated in the Figure.

7.5 Optimize efficiency of identified NCPs

7.5.1 Fundamental investigations on the luminescence of UV emitting LAP ($LaPO_4:Pr^{3+}$) phosphor

The emission spectra of $La_{0.999}Pr_{0.001}PO_4$ at T= 300 K is shown in Figure 45 (λ_{ex}= 193 nm). The broad emission bands are identified as the parity allowed interconfigurational optical transitions emanating from the lowest excited level of the Pr^{3+} $4f^15d^1$ configuration to various states derived from the $4f^2$ electronic configuration. The emission bands labeled 1, 2 and 3 correspond, respectively, to the $4f^15d^1 \rightarrow {}^3H_4$, ${}^3H_5$ and ${}^3H_6$ (${}^3F_2$) optical transitions on the Pr^{3+} ion. Since the initial excited $4f^15d^1$ state is a triplet, these transitions also obey the spin selection rule ($\Delta S=0$).

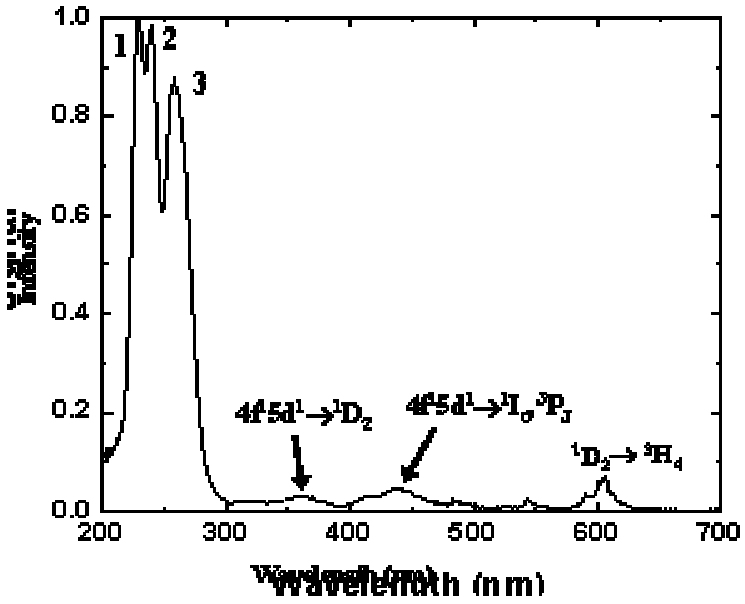

Figure 45: Room temperature emission spectrum of $La_{0.999}Pr_{0.001}PO_4$ at T= 300 K (λ_{ex}= 193 nm).

The weak broad bands centered at about 375 nm and 440 nm are assigned to emission transitions from the $4f^15d^1$ state to the ${}^1D_2$ and the ${}^3P_J$ / ${}^1I_6$ levels of the $Pr^{3+}4f^2$ configuration. The weakness of these bands is related to the fact that the transition probabilities are proportional to ν^3, which thus favors the high-energy bands in the emission spectrum. Note that the $4f^15d^1 \rightarrow {}^3P_J \rightarrow {}^3H_J$ emission process represents a sequential emission of two photons. However, the characteristic lines of the ${}^3P_0 \rightarrow {}^3H_J$

optical transitions in the blue-green are very weak and hardly observed in the room temperature emission spectrum. Instead, weak sharp line emission in the red (600 nm) spectral region is observed. It is possible to associate this transition with the radiative decay of the Pr^{3+} $^1D_2$ state to the $^3H_4$ ground state ($^1D_2 \rightarrow {}^3H_4$). Note that the $^1D_2$ state is also populated through the $4f^15d^1 \rightarrow {}^1D_2$ emission transition and that the $4f^15d^1 \rightarrow {}^1D_2 \rightarrow {}^3H_4$ emission process also represents a sequential emission of two photons. The origins of other features in the room temperature emission spectrum will become clear from the discussion of the emission spectrum at T= 1.6 K.

The physical process responsible for the quenching of $^3P_0$ luminescence and the appearance of $^1D_2$ luminescence is the nonradiative $^3P_J \dashrightarrow {}^1D_2$ transition by multiphonon relaxation (MPR). The MPR process is very efficient because of the high phonon frequency of the host lattice; the archetypal maximum phonon frequency of the P-O stretching vibration of the $[PO_4]^{3-}$ molecular group is in the range of 1200 –1400 cm^{-1} (P-O stretching vibration). The MPR relaxation rate (W_{nr}) can be estimated with the use of the modified energy gap law:

$$W_{nr}\,(T= 0\ K) = \beta_{el} \exp\,[\,-\alpha\,(\Delta E - 2\hbar\omega_{max})] \qquad (1)$$

where $\beta_{el} = 6.2 \times 10^7\ s^{-1}$ and for phosphate glass, $\alpha = 4.7 \times 10^{-3}$ cm. The energy levels of Pr^{3+} in $LaCl_3$ shows an energy gap (ΔE) of ~3700 cm^{-1} between the $^3P_0$ level and the middle of the $^1D_2$ level. Inserting $\hbar\omega_{max}$ =1300 cm^{-1} gives a multiphonon relaxation rate, $W_{nr}\,(T= 0\ K) = 3.5 \times 10^5\ s^{-1}$. This multiphonon relaxation rate should be compared to the radiative relaxation rate (W_R) of Pr^{3+} $^3P_0$ state. The calculated radiative lifetime of the excited Pr^{3+} $^3P_0$ state in $LiPrP_4O_{12}$ and YPO_4 are 43 μs ($W_R = 3.5 \times 10^4\ s^{-1}$) and 70 μs ($W_R = 1.4 \times 10^4\ s^{-1}$), respectively. Consequently, in phosphate host lattices, W_{nr} exceeds or is at least competitive with the radiative relaxation rate of the Pr^{3+} $^3P_0$ state. We, therefore, conclude that the radiationless relaxation by high-energy phonons is responsible for the weakness of the Pr^{3+} $^3P_0$ emission intensity and for the presence of weak emission from the $^1D_2$ state in room temperature emission spectrum of $LaPO_4$: Pr^{3+}. Efficient $^3P_0 \dashrightarrow {}^1D_2$ multiphonon relaxation was also observed in YPO_4: Pr^{3+} with the zircon structure. Further support for the quenching of the Pr^{3+} $^3P_0$ emission by the aforementioned MPR process comes from the following data in the archival literature. While the calculated radiative lifetime of the excited Pr^{3+} $^3P_0$ state in $LiPrP_4O_{12}$ and YPO_4 are 43 μs and 70 μs, the measured room temperature lifetime are 0.1μs and 0.7 μs, respectively. In LaP_5O_{14}:Pr^{3+} a very short $^3P_0$ lifetime was determined (0.12 μs) and found to be independent of the temperature and Pr^{3+} concentration. All of these results suggest that, in phosphates, nonradiative relaxation plays a dominant role in the depopulation of the Pr^{3+} $^3P_0$ state.

We now examine the low temperature emission spectrum. At T = 1.6 K, in addition to the luminescence from the $4f^15d^1$ state, sharp line emission emanating from the $^1S_0$ state are

clearly observed (Figure 46). The $^1S_0 \rightarrow {}^1I_6$ transition appears with the highest intensity. In the photon cascade emission process, the subsequent emission from the $^3P_0$ electronic state produces the second photon. However, as previously discussed, the majority of the second photons are produced from the $^1D_2$ level due to the efficient $^3P_J \dashrightarrow {}^1D_2$ multiphonon relaxation. We assign the broad band centered at 310 nm and sharp line at 540 nm to the luminescence of Ce^{3+} ($5d^1 \rightarrow {}^2F_{5/2}, {}^2F_{7/2}$) and Tb^{3+} ($^5D_4 \rightarrow {}^7F_5$) ions that are present as impurities in our sample.

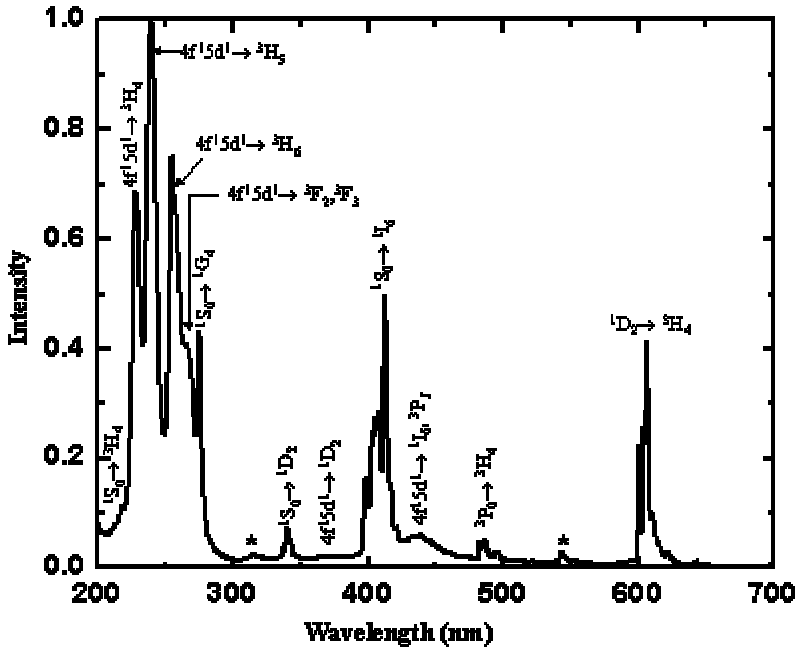

Figure 46: Emission spectrum of $La_{0.999}Pr_{0.001}PO_4$ at T= 1.6 K (λ_{ex}= 193 nm).

Note that at low temperatures, the $^1S_0 \rightarrow {}^1D_2$ optical transition is an additional channel (in addition to the $4f^15d^1 \rightarrow {}^1D_2$ and $4f^15d^1 \rightarrow {}^3P_J \dashrightarrow {}^1D_2$ channels) that populates the $^1D_2$ level. This explains the rather high emission intensity of the $^1D_2 \rightarrow {}^3H_4$ transition at low temperatures.

The $^1S_0 \rightarrow {}^3H_4$ transition can also be observed as a very weak line in the low-resolution emission spectrum exhibited in Figure 46. An attempt was made to determine the energy position of the Pr^{3+} $^1S_0$ state in $LaPO_4$ from a high-resolution emission spectrum, which spanned the $^3H_4$ energy region. As shown in Figure 47, at least seven sharp emission lines can be distinguished in the high-resolution emission spectrum of the $^1S_0 \rightarrow {}^3H_4$ optical transition. The position of the highest energy emission line places the $^1S_0$ level at 46 375 $\pm$ 5 cm^{-1} in $LaPO_4$. The calculated energy position of Pr^{3+} $^1S_0$ state in YPO_4 is 46 152 cm^{-1}.

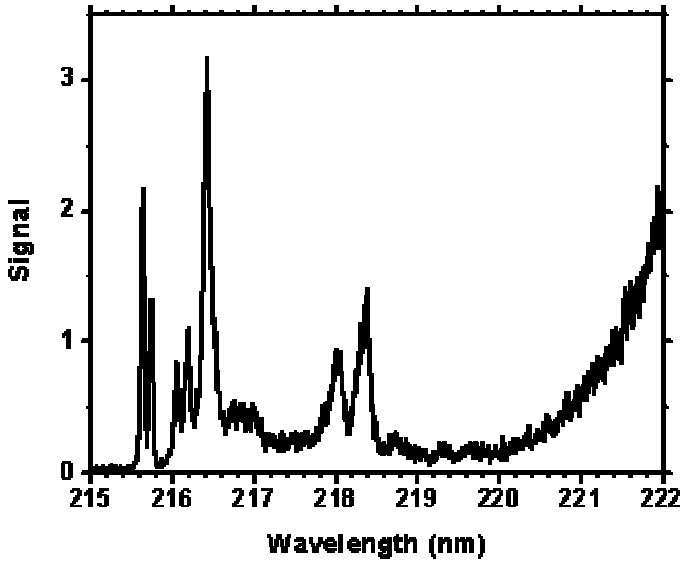

Figure 47: High-resolution emission spectrum of $La_{0.999}Pr_{0.001}PO_4$ at T= 1.6 K (λ_{ex}= 193 nm).

The excitation spectrum of the $4f^15d^1$ emission (λ_{em} = 260 nm) at T= 10 K shows that the lowest energy Pr^{3+} $4f^2 \rightarrow 4f^15d^1$ excitation band in $LaPO_4$ occurs at about 205 nm (48 780 cm^{-1}; see Figure 48). The very low site symmetry (C_1) should completely lift the degeneracy and split the $4f^15d^1$ state into five states. In the room temperature excitation spectrum, at least four bands could be distinguished. The fifth band is either unresolved or obscured by the onset of the host lattice absorption band near 160 nm.

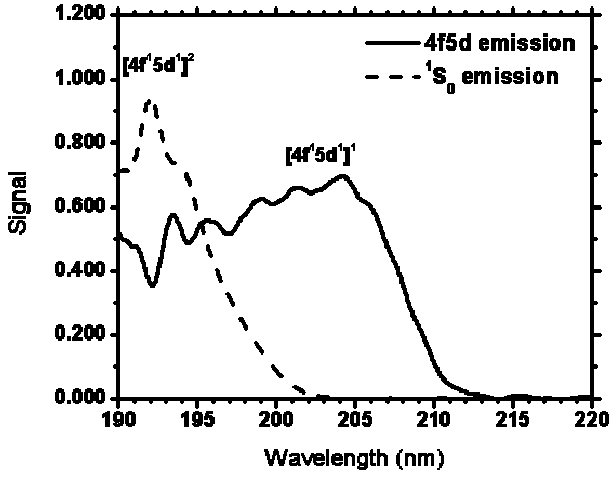

Figure 48: The excitation spectrum of $La_{0.999}Pr_{0.001}PO_4$ at T= 10 K for $4f^15d^1$ and ^1S_o emission

The $4f^15d^1$ emission at 260 nm, on the other hand, is more efficiently excited by the low energy component of the $4f^15d^1$ state, the maximum of which is located at ~205 nm (labeled $[4f^15d^1]^1$). By carefully monitoring the emission spectrum as a function of the excitation wavelength at T= 2 K, it was determined that $^1S_0$ luminescence appears for $\lambda \leq$ 204 nm ($E \geq 49\ 000\ cm^{-1}$) whereas interconfigurational optical transitions appear in the emission spectrum for $\lambda \leq 211$ nm ($E \geq 47\ 400\ cm^{-1}$). This is in agreement with the observed excitation spectra when the emissions from the respective states are monitored.

The simultaneous occurrence of the $4f^15d^1$ and the $^1S_0$ luminescence at low temperatures may be explained by assuming that there are two distinct Pr^{3+} sites in the $LaPO_4$ host lattice. In one of these sites, the lowest energy component of the crystal field split $4f^15d^1$ state is located above the $^1S_0$ level (46 375 cm^{-1}). We hold this site, [Pr^{3+} (A)], responsible for emission from the $^1S_0$ state. For the other site, [Pr^{3+}(B)], the crystal field split components of the $4f^15d^1$ state are energetically below that of the $^1S_0$ state. This Pr^{3+} site is responsible for emission from the $4f^15d^1$ state. The different excitation spectra recorded when monitoring the $4f^15d^1$ and the $^1S_0$ luminescence supports this model. Since there is considerable overlap of the excitation spectra at high energy, the concurrent occurrence of $4f^15d^1$ and the $^1S_0$ luminescence may be explained by the simultaneous excitation of the two centers by 193 nm-UV radiation.

In the two site model, the quenching of the $^1S_0$ emission intensity and the shortening of the lifetime with increasing temperature (to be discussed below) can be attributed to energy transfer from the high energy [Pr^{3+} (A); with dominant $^1S_0$ emission] site to the lower energy [Pr^{3+}(B); with dominant $4f^15d^1$ emission] site or to the thermal population of the $4f^15d^1$ levels associated with the [Pr^{3+} (A)] site.

However, we do not have further experimental proof nor can we hypothesize for the origin of two distinct Pr^{3+} sites with markedly different optical properties in the $LaPO_4$ host lattice. As previously noted, the $LaPO_4$ crystal structure offers a single site for the Pr^{3+} ion and since there is no requirement for charge compensation, structural factors cannot be the reason for the occurrence of two different sites. We note that the need for charge compensation in certain host lattices leads to the formation of sites with varying crystal field strengths that results in the simultaneous emission from the $^1S_0$ and $4f^15d^1$ states. Further, the optical properties of samples with higher Pr^{3+} concentrations (up to 5 mole%) are similar to the low-doped samples. Further, as will be shown below, single exponential decay curves have been obtained for the $^1S_0$ state in the investigated temperature range. These results suggests that the temperature dependence of the $^1S_0$ lifetime and emission intensity should be modeled in terms of a model that pertains to a single and well defined site for the Pr^{3+} ion in the $LaPO_4$ host lattice.

It is clear from the excitation spectrum that population of both the $^1S_0$ and $4f^15d^1$ states is attained when exciting into the higher energy $[4f^15d^1]^2$ state (λ_{ex}=193 nm). At each temperature, the population of the states and the probability of spontaneous decay

determines the $^1S_0$ and the $[4f^l5d^1]^1$ luminescence intensity. Experimental results pertaining to the temperature dependence of the $^1S_0$ lifetime and emission intensity and the $[4f^l5d^1]^1$ emission intensity indicate that the population distribution attained from the feeding of the two levels via the upper $[4f^l5d^1]^2$ state does not appreciably vary with temperature. For example, under excitation by 193 nm-UV photon, the emission intensity of the $[4f^l5d^1]^1$ state remains fairly constant through out the investigated temperature range. Further, within experimental error, the temperature dependence of the $^1S_0$ lifetime and the emission intensity are identical. This strongly suggest that the population distribution attained from the upper $[4f^l5d^1]^2$ state does not vary with temperature.

As shown in Figure 49, the $^1S_0$ decay curve is a single exponential over the entire temperature range. Figure 7 exhibits the variation of the $^1S_0$ lifetime as a function of increasing temperature. The $^1S_0$ lifetime (145 ns) and the emission intensity are found to be temperature independent in the range of 1.6-25 K. The radiative decay rate of the $^1S_0$ state is thus $6.89*10^6$ s^{-1}. The radiative lifetime of 145 ns in $LaPO_4$ is one of the shortest observed for the Pr^{3+} $^1S_0 \rightarrow {}^1I_6$ optical transition in solids. The short lifetime, which is uncharacteristic of a typical $4f^n \rightarrow 4f^n$ optical transition, becomes possible due to the mixing of the $4f^l5d^1$ wave function in the $^1S_0$ state. This suggests the proximity of the $^1S_0$ and the $4f^l5d^1$ states so that the shortening in the $^1S_0$ radiative lifetime is due to increased $4f^l5d^1$ character in the $^1S_0$ level.

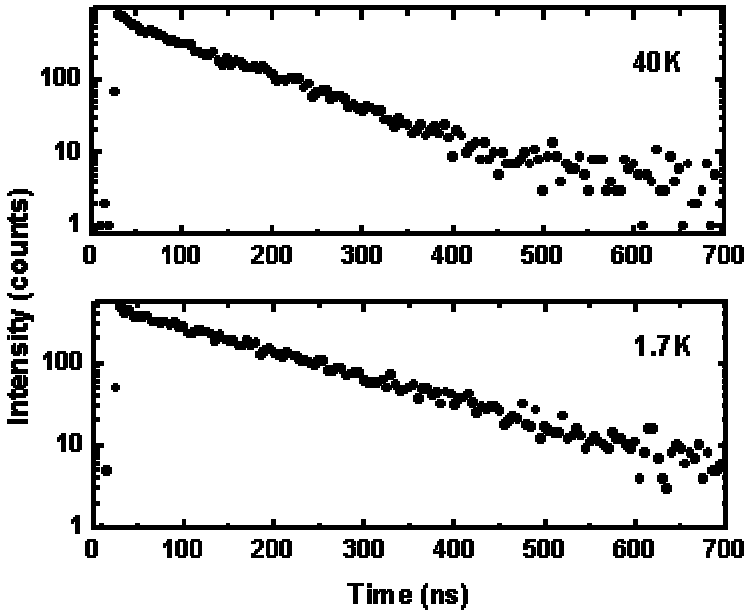

Figure 49: The $^1S_0$ decay curves in $La_{0.999}Pr_{0.001}PO_4$ at T= 10 K and T= 1.7 K

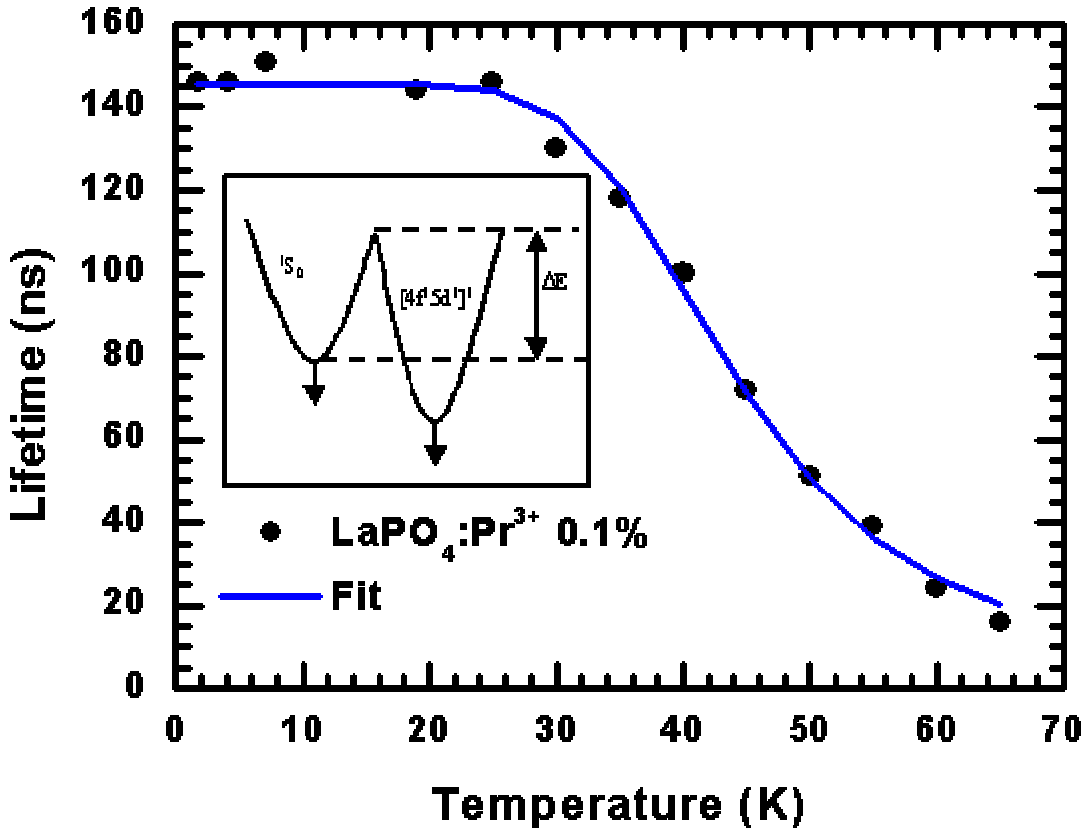

Figure 50: The temperature dependence of the $^1S_0$ relaxation time in $La_{0.999}Pr_{0.001}PO_4$ (see text for the model)

Figure 50 shows the temperature dependence of the ^1S_o relaxation time as a function of temperature. For T < 25 K, we can reasonably assume that the relaxed excited states of the $^1S_0$ and $4f^15d^1$ configurations are disconnected. The $^1S_0$ lifetime shortens rapidly as the temperature is raised beyond 25 K. The lifetime is shortened from 145 ns at T= 1.6 K to 10 ns at T= 60 K. This indicates the onset of nonradiative transitions within the $^1S_0$ level for T > 25 K (Figure 50). We note that the large energy separation of ~24 000 cm^{-1} between the $^1S_0$ and the next-lower level of the $4f^2$ prevents nonradiative relaxation by multiphonon emission. Since $^1S_0$ decay curves are single exponential over the entire temperature range investigated, the rapid quenching of the $^1S_0$ lifetime and the emission intensity for T > 25 K must have a different physical origin.

For T > 25 K, the decay rate of the $^1S_0$ state can be given as:

$$1/\tau_S = 1/\tau_r + 1/\tau_{nr} \qquad (2)$$

where $1/\tau_{nr}$ is the characteristic nonradiative decay rate and $1/\tau_r$ is the radiative decay rate. The nonradaitive decay rate is generally assumed to vary as:

$$1/\tau_{nr} = C \exp(-\Delta E/kT) \quad (3)$$

where k is the Boltzmann constant. From equations (2) and (3) we can write

$$1/\tau_{nr} = [1/\tau_S - 1/\tau_r] = C \exp(-\Delta E/kT) \quad (4)$$

Hence, the plot of ln $[1/\tau_S - 1/\tau_r]$ against 1/T should be a straight line from which the values of ΔE (in cm^{-1}) and C (in s^{-1}) can be determined. The plot of ln $[1/\tau_S - 1/\tau_r]$ against 1/T ($1/\tau_r = 6.89*10^6$ s^{-1} obtained from T < 25 K lifetime data) is indeed a straight line yielding $C= 1.5*10^9$ s^{-1} and $\Delta E = 165$ cm^{-1}. The drawn line in Figure 50 is the fit to the equation: $\tau = \tau_r / 1+ [\tau_r /\tau_{nr}] \exp(-\Delta E/kT)$ with $1/\tau_r = 6.89*10^6$ s^{-1}, $1/\tau_{nr} = 1.5*10^9$ s^{-1} and $\Delta E = 165$ cm^{-1}.

The values of ΔE (in cm^{-1}) and C (in s^{-1}) can also be determined from the temperature dependence of the $^1S_0$ emission intensity. This, however, requires the deconvolution of the $^1S_0$ emission transitions from the stronger $4f^15d^1$ transitions over the entire temperature range. By focusing our attention on the broadband $4f^15d^1$ emission, it was noted that intensity distribution did not change significantly over the entire range of temperature. It was further noted that no sharp features of the $^1S_0$ occur at temperatures above 150 K. Under these conditions, the emission spectra, which represent the optical transitions from the $^1S_0$ state, were obtained by subtracting the background intensity from the broad $4f^15d^1$ emission. Thus, a series of $^1S_0$ emission plots were obtained for temperatures from 100 K to 1.6 K. In this way, the temperature dependence of the $^1S_0$ emission intensity was obtained from these corrected spectra.

For T > 25 K, the $^1S_0$ emission intensity is related to the radiative decay time by:

$$I_0/I = \tau_r /\tau_S \quad (5)$$

Here I_0 is the emission intensity at T= 1.6 K and I is the emission intensity at the specified temperature. Substituting in equation 1 and rearranging gives:

$$1/\tau_{nr} = [1/\tau_S - 1/\tau_r] = [1/\tau_r (I_0/I - 1)] \quad (6)$$

Again, assuming that $1/\tau_{nr}$ varies as given in equation (2), we find that the plot of ln $[1/\tau_r (I_0/I) - 1]$ versus 1/T should be a straight line from which the values of ΔE (in cm^{-1}) and C

(in s^{-1}) can be determined. This analysis yields C= $1.9*10^9$ s^{-1} and ΔE = 164 cm^{-1}, which is in excellent agreement with the values derived from the temperature dependence of the lifetime data.

We have now determined two quantities of importance, the activation energy ΔE and the (nonradiative) thermal quenching rate. Since kT ≅ 200 cm^{-1} at room temperature it is clear that there is a very high probability of classically surmounting the potential barrier (ΔE=165 cm^{-1}). This explains the absence of $^1S_0$ luminescence in the room temperature emission spectrum of $LaPO_4$: Pr^{3+}. To the best of our knowledge, the energy barrier of 165 cm^{-1} between the Pr^{3+} $^1S_0$ and $4f^15d^1$ is one of the smallest observed in all host lattice that have been reported in the archival literature.

The total emission efficiency ($4f^15d^1$+$^1S_0$) is determined to be fairly constant from 1.6 K to 250 K. Therefore, the rapid decrease in the $^1S_0$ lifetime and emission intensity with increasing temperature does not result in enhanced nonradiative losses. This lead us to conclude that with increasing temperature, the $^1S_0$ state simply populates the lowest energy $[4f^15d^1]^1$ state thereby keeping the total quantum efficiency constant through the temperature range. Hence, ΔE measures the classical energy required for the electron in the $^1S_0$ potential well to surmount the potential barrier (165 cm^{-1}) and crossover nonradiatively to the $[4f^15d^1]^1$ potential well. The inset in Figure 50 shows the coupled parabolas of the $^1S_0$ and $4f^15d^1$ state and defines the activation energy (ΔE). Summarizing, for T > 25 K, the $^1S_0 \rightarrow {}^1I_6$ luminescence lifetime and the emission intensity decreases because of the enhanced nonradiative transitions due to the $^1S_0$ - $[4f^15d^1]^1$ internal conversion. This explains the complete absence of the $^1S_0$ emission in the room temperature emission spectrum.

In Figure 51 we have schematically constructed a single configurational coordinate (CC) diagram to explain the salient features of the Pr^{3+} luminescence in $LaPO_4$. The argument for placing the minimum of the $[4f^15d^1]^1$ state energetically below that of the $^1S_0$ state is now presented. The low temperature excitation spectrum clearly indicates that it is possible to excite the luminescence of the $[4f^15d^1]^1$ state selectively. Hence, if we only create the $[4f^15d^1]^1$ by selective excitation in the low energy $[4f^15d^1]^1$ band then the $^1S_0$ emission lines would not appear in the low temperature emission spectrum. In the CC diagram of Figure 50, this is shown by the (excitation) transition from A to B. Since the point C, which represents the minimum of the $[4f^15d^1]^1$ parabola, is located at lower energy relative to the minimum of the $^1S_0$ parabola, we would expect broadband interconfigurational $[4f^15d^1]^1 \rightarrow 4f^2$ emission transitions at the lowest temperatures. In the reverse situation in which the $[4f^15d^1]^1$ minimum is situated at higher energy relative to the $^1S_0$ minimum, the Pr^{3+} ion would emit predominantly from the $^1S_0$ state at the lowest temperatures. This is the situation described by the Pr^{3+} energy level diagram of Figure 1 and observed in numerous materials where the crystal field split components of the $4f^15d^1$ state are located energetically above the $^1S_0$ level. Taking the analysis further, if the $4f^15d^1$ state is located above the $^1S_0$ state and if the energy separation between the two states were not large, then any $4f^15d^1$ luminescence would arise from the thermal population of the $4f^15d^1$ state via the $^1S_0$ state.

Even in this situation we would have expected finite intensity for the $^1S_0$ emission at room temperature in $LaPO_4$: Pr^{3+}. Because our experimental data differs entirely from the expectations of the $4f^15d^1$ configuration being located above the $^1S_0$ level, we conclude that the relaxed excited state of the $4f^15d^1$ manifold is located energetically below that of the $^1S_0$ level in $LaPO_4$: Pr^{3+}.

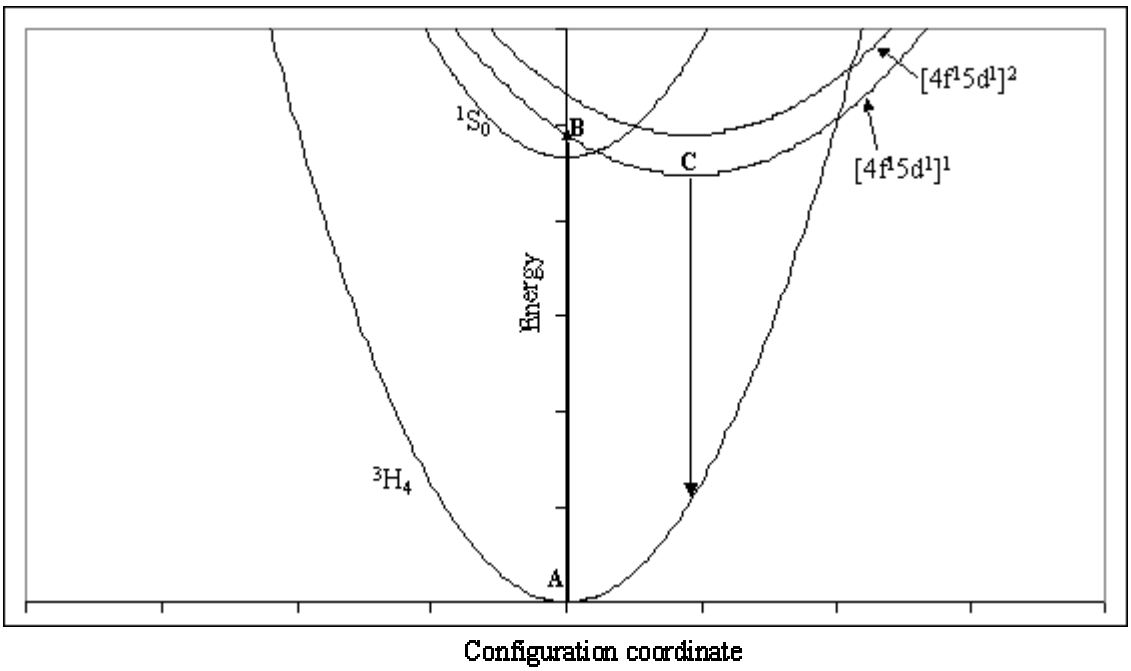

Figure 51: A schematic configuration coordinate model for the luminescence of Pr^{3+} in $LaPO_4$

It is not often that we encounter a situation where $^1S_0$ emission is observed when the (relaxed) $4f^15d^1$state is energetically below the $^1S_0$ state. To the best of our knowledge this constitutes the first observation of the luminescence from the $^1S_0$ level under the aforementioned condition. The reason for the positioning of the relaxed $4f^15d^1$ state below that of the $^1S_0$ state in $LaPO_4$ is the following. The excitation spectrum (unrelaxed state or ground state geometry) shows that the lowest energy component of the $[4f^15d^1]^1$ state (48 800 cm^{-1}) is located energetically above the $^1S_0$ level (46 375 cm^{-1}). Note that under this condition we would expect to observe $^1S_0$ luminescence at room temperature. However, we have yet to consider the relaxation process that occurs after excitation. In the excited $4f^15d^1$ state, the geometry of the Pr^{3+} site in $LaPO_4$ relaxes significantly. This is evidenced by the rather large Stokes shift of the emission (~ 5000 cm^{-1}). The large Stokes shift, which results in a significant lowering of the $[4f^15d^1]^1$ edge, is responsible for the $[4f^15d^1]^1$ level being located below the $^1S_0$ state. Note that in the configurational coordinate model of Figure 51, the condition for the observation of emission from the $^1S_0$

state at room temperature is not only that the point B should be energetically above the $^1S_0$ state, but also that the equilibrium distances of the $^3H_4$ ground state and the $4f^15d^1$ state is small. In other words, the Stokes shift of the Pr^{3+} emission should be small.

7.5.2 Luminescence from the Pr^{3+} $4f^15d^1$ and $^1S_0$ states in $LiLaP_4O_{12}$

As a part of research activity pertaining to further enhancing our knowledge of the quantum splitting behavior of the Pr^{3+} ion, we examined the optical properties of Pr^{3+} activated $LiLaP_4O_{12}$. The host material crystallizes in the monoclinic symmetry with space group C 2/c. The La^{3+} ions (site symmetry C_1) occur in dodecahedral coordination (eight coordination).

The excitation spectrum of $LiLa_{0.999}Pr_{0.001}P_4O_{12}$ at T= 10 K is shown in Figure 52 (λ_{em}= 406 nm, which corresponds to the $^1S_0 \rightarrow {}^1I_6$ optical transition). The broad excitation bands are identified as the parity allowed interconfigurational optical transitions originating from the $^3H_4$ ground state to the crystal field split excited $4f^15d^1$ states. However, it should be noted that the interaction of the 4f electron and the 5d electron can give rise to many 4f5d levels (interconfigurational mixing).

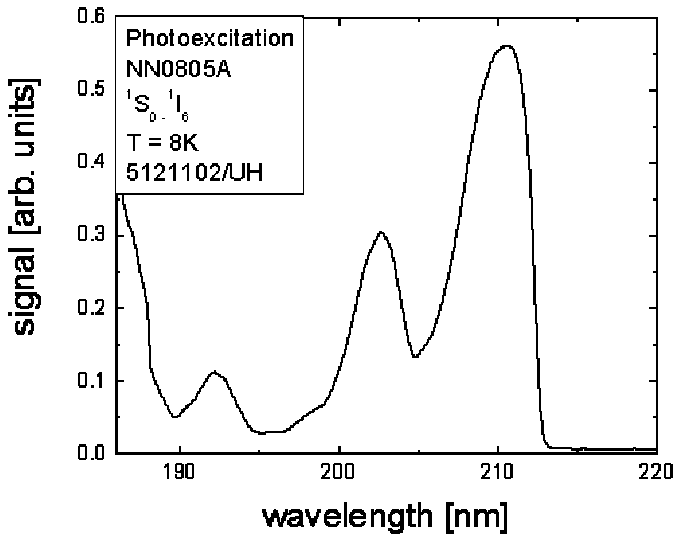

Figure 52: The excitation spectrum of $LiLa_{0.999}Pr_{0.001}P_4O_{12}$ at T= 10 K (λ_{em}= 406 nm)

The corresponding emission spectrum of $LiLa_{0.999}Pr_{0.001}P_4O_{12}$ at various temperatures is shown in Figure 53 (λ_{ex}= 210 nm). The broad emission bands in the 200 nm- 250 nm

wavelength region, labeled 1, 2 and 3 correspond to the $4f^15d^1 \rightarrow {}^3H_4$, $^3H_5$ and $^3H_6$ ($^3F_2$) optical transitions on the Pr^{3+} ion. Since the initial excited $4f^15d^1$ state is a triplet these transitions also obey the spin selection rule ($\Delta S=0$). Further, sharp line emission transitions emanating from the $^1S_0$ state are also clearly observed in the emission spectrum. The $^1S_0 \rightarrow {}^1I_6$ transition appears with the highest intensity. A weak line emission centered at ~ 310 nm is identified as being transition associated with the Gd^{3+} $^3P_J \rightarrow {}^8S_{7/2}$ emission transition, which is present as impurities in our sample.

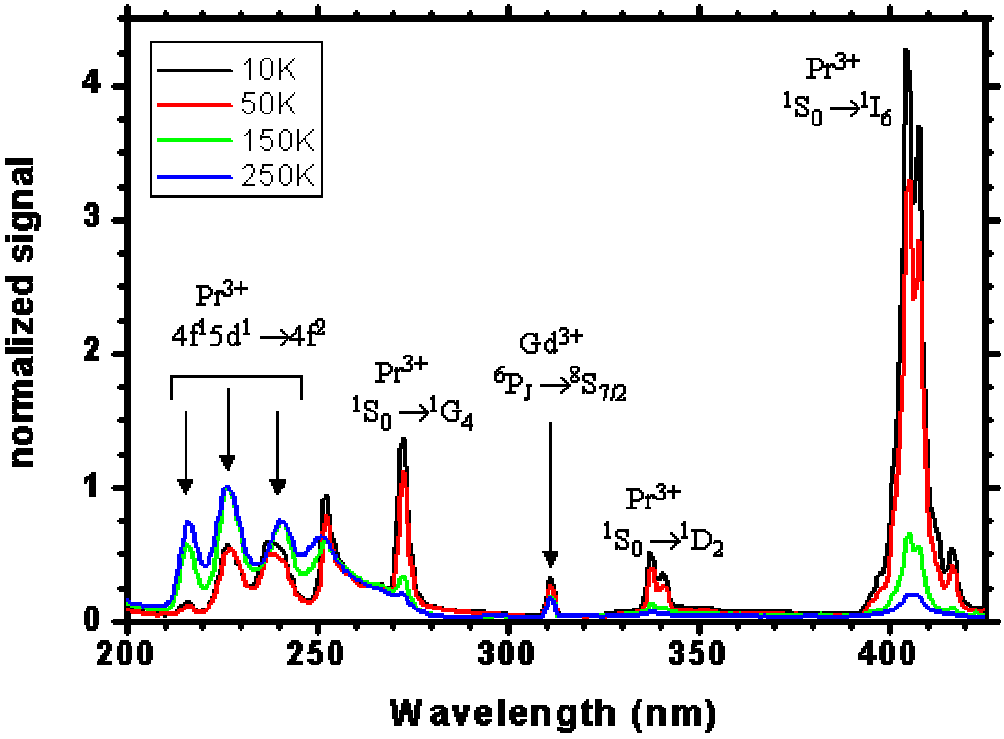

Figure 53: The emission spectra of $LiLa_{0.999}Pr_{0.001}P_4O_{12}$ at various temperatures (λ_{ex}= 210 nm)

In is clear from Figure 53 that the emission intensity of the $^1S_0 \rightarrow {}^1I_6$ transition decreases with increasing temperature while the $4f^15d^1 \rightarrow 4f^2$ interconfigurational optical transitions gains intensity. To derive the activation energy for the quenching of the $^1S_0 \rightarrow {}^1I_6$ transition, the temperature dependence of the lifetime of this transition was measured. The $^1S_0$ decay curve was found to be a single exponential over the entire temperature range.

Figure 54 exhibits the variation of the $^1S_0$ lifetime as a function of increasing temperature. The $^1S_0$ lifetime (600 ns) was found to be temperature independent in the range of 8-70 K. The radiative decay rate of the $^1S_0$ state is thus $1.66*10^6$ s^{-1}. This short lifetime, which is uncharacteristic of a typical $4f^n \rightarrow 4f^n$ optical transition, becomes possible due to the mixing of the $4f^15d^1$ wave function in the $^1S_0$ state. For T < 70 K, we can reasonably assume that the relaxed excited states of the $^1S_0$ and $4f^15d^1$ configurations are disconnected. The $^1S_0$ lifetime shortens rapidly as the temperature is raised beyond 70 K. The lifetime is shortened from 600 ns at T= 8 K to 100 ns at T= 160 K. This indicates the onset of nonradiative transitions within the $^1S_0$ level for T > 70 K. We note that the large energy separation of ~24 000 cm^{-1} between the $^1S_0$ and the next-lower level of the $4f^2$ prevents nonradiative relaxation by multiphonon emission. The drawn line in Figure 53 is the fit to the equation: $\tau = \tau_r / 1+ [\tau_r / \tau_{nr}] \exp(-\Delta E/kT)$ with $1/\tau_r = 1.66*10^6$ s^{-1}, $1/\tau_{nr} = 4.24*10^8$ s^{-1} and $\Delta E = 0.05$ eV (438 cm^{-1}).

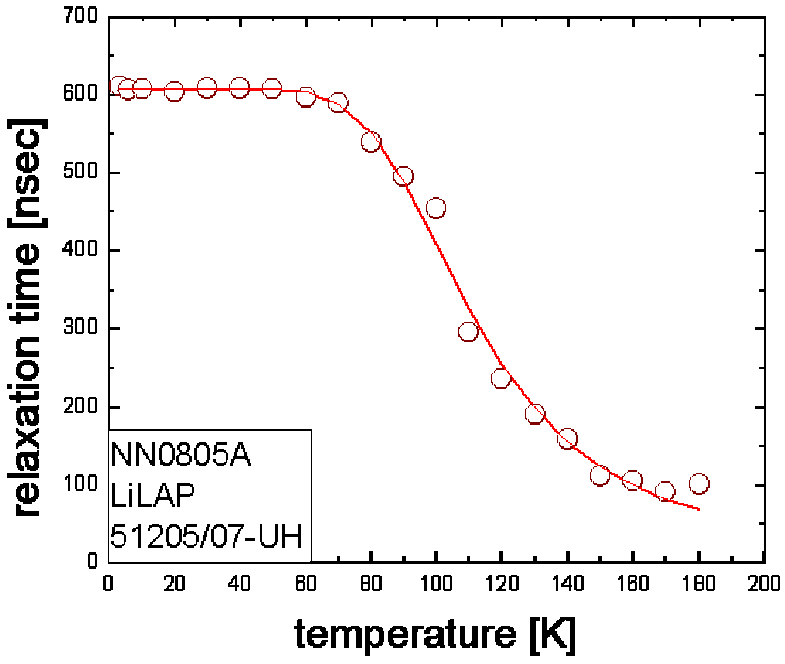

Figure 54: The temperature dependence of the Pr^{3+} $^1S_0 \rightarrow {}^1I_6$ (λ_{em} = 405 nm) lifetime in $LiLaP_4O_{12}$. The excitation wavelength was 193 nm. The full circles are the experimental points and the solid curve is the theoretical fit (see text).

Since the energy separation between the $4f^15d^1$ and $^1S_0$ states is not large, the quenching of the $^1S_0$ emission transitions with increasing temperature can be attributed to the thermal population of the $4f^15d^1$ state via the $^1S_0$ state. The activation energy of 0.05 eV represents the energy barrier between the $^1S_0$ state and the lowest energy component of the $4f^15d^1$ configuration.

Note that even at the lowest temperatures, emission from the $4f^15d^1$ configuration is observed in $LiLa_{0.999}Pr_{0.001}P_4O_{12}$. Since we can define the luminescence intensity from level *i* to the ground state (*0*) as $I_{i0} = h\nu_{i0}P_r n_i$ where $h\nu_{i0}$ is the energy of the photon emitted, P_r is the radiative decay time and n_i is the population of the *i* state, the luminescence from the $4f^15d^1$ state can arise from the fact that the typical radiative decay rate of the $4f^15d^1$ state ($\sim 5*10^7\ s^{-1}$) is roughly ten times the radiative decay rate of the $^1S_0$ state ($1.66*10^6\ s^{-1}$).

In conclusion, the temperature dependence of the Pr^{3+} luminescence in $LiLaP_4O_{12}$ has been investigated. The simultaneous luminescence from the $4f^15d^1$ and the $^1S_0$ states has been observed at all temperatures (T= 8 K- 300 K). With increasing temperature the emission from the $4f^15d^1$ state gains intensity at the expense of emission from the $^1S_0$ state. The $^1S_0$ lifetime shortens rapidly as the temperature is raised beyond 70 K. These results are explained on the basis of thermal population of the $4f^15d^1$ state by the $^1S_0$ state. The energy barrier between the $^1S_0$ state and the lowest energy component of the $4f^15d^1$ state is 0.05 eV.

8. SUMMARY

This section will be devoted to a brief summary of the status of this work and some considerations for future research and development.

From our investigations of the requirement of the particle size we conclude that the achievement of improved lamp output in the hybrid phosphor concept is only possible if the particle size of the nanocrystalline phosphor is less than 100 nm. This particle size reduces the scattering of the 254 nm radiation.

Our work to develop suitable nanocrystalline phosphors started with the known oxide quantum splitting and UV emitting phosphors. This work was very successful. We demonstrated several synthesis techniques for oxides, phosphate and borates host materials. The synthesis resulted in the production of high quality nanocrystalline materials that crystallizes in the desired phase and with the desired particle size. We also optimized the synthesis of three phosphors, SAP ($SrAl_{12}O_{19}:Pr^{3+}$), LAP ($LaPO_4$: Pr^{3+}) and $LaB_3O_6:Pr^{3+}$. For the first time we demonstrated the occurrence of quantum splitting from the Pr^{3+} ion in nanocrystalline SAP and LaB_3O_6 phosphors. Various synthesis procedures were applied to obtain high quality nano phosphors. The synthesis procedure based on the surfactant technique yielded the best results in terms of the quality and size of the nano particles. Detailed optical characterization (excitation/emission spectra, temperature dependence of the relaxation time of the $^1S_0$ level) clearly showed the absence of additional quenching pathways for the Pr^{3+} ion in nano crystalline SAP samples. This indicated the high quality of the particles produced by this synthesis technique.

In collaboration with our subcontractor we demonstrated the feasibility for the manufacture of nanocrystalline phosphors. We demonstrated quantum splitting in these phosphors and determined that the vacuum ultraviolet-excited emission spectra of these phosphors was identical to that reported for large size materials. These results are very encouraging. Hence, with regards to the manufacturability of these materials, we would strongly encourage the continued exploration and refinement in the synthesis that are being developed by our subcontractors within the program.

Using our set of rules for identifying materials in which Pr^{3+} can either quantum split or exhibit efficient UV emission has lead to the discovery of three new potential host materials. Our fundamental investigations into the luminescence of LAP ($LaPO_4:Pr^{3+}$) and $LiLaP_4O_{12}:Pr^{3+}$ has helped to further codify a set of rules for the host lattice that support efficient quantum splitting at room temperature. Consequently, with regards to the discovery of new phosphors we would also strongly recommend the continued exploration and refinement of the phosphor design rules that are developed within the previous DOE funded program and which were further substantiated within this program.

We worked on developing coatings methodology that would yield hybrid phosphors with high quantum efficiency. This work was also very successful and also led to significant insights into issues pertaining to coatings and their possible solution. Improvements in

the coating technology has now led to hybrid phosphor systems with high quantum efficiency under 254 nm excitation.

In fluorescent lamp testing, we demonstrated improved lumen output (lumes per watt) and lumen maintenance of the commercial $YVO_4:Eu^{3+}$ phosphor that were coated with the nano LAP phosphor. At 100 hours of burning, the uniformly coated YVO_4 phosphors exhibited a ~7% increase in the LPW relative to the uncoated phosphor.

We demonstrated that the critical quantity to control in obtaining enhanced lumen output of the hybrid phosphor is the minimum or no scattering of the 254 nm radiation by the outer nano phosphor coating. This was clearly evidenced in the lamp test results of the coated YEO phosphor. The YEO phosphor also exhibited serious problems in water based suspensions. The particles aggregated in suspension so that the lamp coatings were not uniform. This lead to reduced lumen output of the coated phosphor relative to the commercial (uncoated) phosphors. The suspension problem was not resolved during the course of this work. A clear dependence of the lumen output on the 254 nm reflectivity of the hybrid phosphor was noted. This work showed that provided that condition of minimum scattering of the 254 nm photons by the outer nano coating is satisfied, we can expect improved lumen output from the hybrid phosphor system.

9.0 US PATENTS AND APPLICATIONS

1. **"Light sources with nanometer-sized VUV radiation-absorbing phosphors", US6982046 B2,** Application No. **US2003674376A** Filed **20031001** Published **20060103**
Inventors: Srivastava, Alok Mani, Setlur, Anant Achyut, Loureiro, Sergio Paulo Martins, Williams, Darryl Stephen, Manoharan, Mohan

2. "Method for making phosphors", US20060222757 A1, Application No. US200596502A **Filed** 20050331 **Published** 20061005

Inventors: Loureiro, Sergio, Stoklosa, Stanley, Setlur, Anant, Srivastava, Alok, Manoharan, Mohan

10.0 EXTERNAL PUBLICATIONS AND PRESENTATIONS

206th MEETING OF THE ELECTROCHEMICAL SOCIETY
Honolulu, Hawaii, October 3-8, 2004

1. H. A. Comanzo, A. A. Setlur, A. M. Srivastava, P. Schmidt and U. Happek, " Optical Properties of the Quantum Cascade nanocrystalline phosphor $SrAl_{12}O_{19}:Pr^{3+}$", Abstract # 2078
2. H. A. Comanzo, A. A. Setlur, A. M. Srivastava, M. Hannah, U. Happek and W. W. Beers, " Effect of Ga^{3+} addition on the Quantum Cascade process in $SrAl_{12}O_{19}:Pr^{3+}$", Abstract # 2063
3. M. Hannah, U. Happek, A. M. Srivastava, H. A. Comanzo and A. A. Setlur, " Does Pr^{3+} $^1S_0$ level transfer energy to Gd^{3+} in $SrAl_{12}O_{19}:Pr^{3+}$", Abstract # 2065
4. P. Schmidt, U. Happek, A. M. Srivastava, H. A. Comanzo, A. A. Setlur and W. W. Beers, " Anomaleous optical Properties of $LaPO_4:Pr^{3+}$ at low temperatures", Abstract # 2062
5. A. M. Srivastava, "The quest for multiphoton emitting phosphors", Abstract # 2059

208th MEETING OF THE ELECTROCHEMICAL SOCIETY
Los Angeles, California, October 16-21, 2005

1. A. Setlur, A. Srivastava, H. Comanzo, U. Happek and P. Schmidt, "Cross-Relaxation between the $^3P_0$ level of Pr^{3+} and Ce^{3+}", Abstract # 1121
2. P. A. Schmidt, U. Happek, H. Comanzo, A. Setlur, A. Srivastava and W. Beers, "4f5d, $^3P_0$ Level Assignment from Anomalous Optical Properties of $LaPO_4:Pr^{3+}$ at low temperatures", Abstract # 1122
3. P. A. Schmidt, U. Happek, H. Comanzo, A. Setlur, A. Srivastava, W. Beers, R. Garaas and S. Loureiro, " Characterization of nano sized $LaPO_4:Pr^{3+}$", Abstract # 1124

210th MEETING OF THE ELECTROCHEMICAL SOCIETY
Cancun, Mexico, October 29-November 3, 2006

1. P. Schmidt, A. M. Srivastava, A. Setlur, H. Comanzo, U. Happek, J. Hughes and M. Hannah, " On the Luminescence of Pr^{3+} in $LiLaP_4O_{12}$" Abstract # 2170
2. R. Partch and T. Tannahill, " Studies on Metal Oxide Composite particles for Improved Lighting Efficiency", Abstract # 2185

PUBLICATIONS

1. Sergio M. Loureiro, Anant Setlur, William Heward, Seth T. Taylor, Holly Comanzo, Mohan Manoharan and Alok Srivastava, " First Observation of Quantum Splitting Behaviour in Nanocrystalline $SrAl_{12}O_{19}$: Pr, Mg Phosphor", Chemistry of Materials, 17 (2005) 3108-3113